Article

Neuron

Precise Synaptic Balance in the Zebrafish Homolog of Olfactory Cortex

Highlights

- Odor responses in zebrafish olfactory cortex support a "balanced state"
- Synaptic conductances are balanced on fast timescales and in coding space
- This implies co-tuning of excitatory and inhibitory synaptic inputs
- Precise balance may stabilize memory patterns and support fast classification

Authors

Peter Rupprecht, Rainer W. Friedrich

Correspondence

peter.rupprecht@fmi.ch (P.R.),
rainer.friedrich@fmi.ch (R.W.F.)

In Brief

Rupprecht and Friedrich find that a transient balanced state is established in the zebrafish homolog of olfactory cortex during an odor response. The balance is maintained on short timescales (tight balance) and in stimulus space (detailed balance) and can stabilize activity patterns in coding space while preserving a high temporal bandwidth.

Rupprecht & Friedrich, 2018, Neuron *100*, 1–15
November 7, 2018 © 2018 Elsevier Inc.
https://doi.org/10.1016/j.neuron.2018.09.013

CellPress

Please cite this article in press as: Rupprecht and Friedrich, Precise Synaptic Balance in the Zebrafish Homolog of Olfactory Cortex, Neuron (2018), https://doi.org/10.1016/j.neuron.2018.09.013

Neuron
Article

CellPress

Precise Synaptic Balance in the Zebrafish Homolog of Olfactory Cortex

Peter Rupprecht[1,2,*] and Rainer W. Friedrich[1,2,3,*]
[1]Friedrich Miescher Institute for Biomedical Research, Maulbeerstrasse 66, 4058 Basel, Switzerland
[2]Faculty of Natural Sciences, University of Basel, 4003 Basel, Switzerland
[3]Lead Contact
*Correspondence: peter.rupprecht@fmi.ch (P.R.), rainer.friedrich@fmi.ch (R.W.F.)
https://doi.org/10.1016/j.neuron.2018.09.013

SUMMARY

Neuronal computations critically depend on the connectivity rules that govern the convergence of excitatory and inhibitory synaptic signals onto individual neurons. To examine the functional synaptic organization of a distributed memory network, we performed voltage clamp recordings in telencephalic area Dp of adult zebrafish, the homolog of olfactory cortex. In neurons of posterior Dp, odor stimulation evoked large, recurrent excitatory and inhibitory inputs that established a transient state of high conductance and synaptic balance. Excitation and inhibition in individual neurons were co-tuned to different odors and correlated on slow and fast timescales. This precise synaptic balance implies specific connectivity among Dp neurons, despite the absence of an obvious topography. Precise synaptic balance stabilizes activity patterns in different directions of coding space and in time while preserving high bandwidth. The coordinated connectivity of excitatory and inhibitory subnetworks in Dp therefore supports fast recurrent memory operations.

INTRODUCTION

Information processing in the brain depends on the relative tuning of inhibitory and excitatory synaptic inputs to individual neurons. Antagonistic tuning of excitation and inhibition can shape complementary domains of receptive fields such as on and off domains of neurons in visual cortex (Hubel and Wiesel, 1962). Alternatively, the response of a neuron may be determined primarily by the tuning of the excitatory input while inhibition is global. This organization is consistent with broad tuning of inhibitory neurons and may normalize or set a threshold for population activity (Isaacson and Scanziani, 2011). In a third scenario, tuning of inhibition and excitation is uncorrelated, as in models of randomly connected networks (Denève and Machens, 2016; Shadlen and Newsome, 1994; van Vreeswijk and Sompolinsky, 1996). Finally, inhibitory and excitatory synaptic inputs can be co-tuned (Anderson et al., 2000; Dorrn et al., 2010; Tan et al., 2004, 2011; Wehr and Zador, 2003) which may stabilize network dynamics (Denève and Machens, 2016; Hennequin et al., 2014, 2017; Rubin et al., 2017; Vogels et al., 2011). Insights into the tuning of excitatory and inhibitory inputs to individual neurons are thus important to understand the computational functions of a neural circuit.

Circuit function also depends on the strength and dynamics of synaptic inputs. When the total input is modest, action potential generation requires an imbalance between strong excitatory input and weak inhibitory input. Alternatively, neuronal networks may operate in a "balanced state" that emerges when excitation and inhibition are both strong and establish an average membrane potential near spike threshold (Murphy and Miller, 2009; Renart et al., 2010; Shadlen and Newsome, 1994; van Vreeswijk and Sompolinsky, 1996). Action potentials are thus generated by fluctuations in the synaptic balance that may be generated by the internal dynamics of the network or by external inputs. Balanced network models can reproduce irregular firing patterns of cortical neurons and have become important general models of neuronal circuits (Denève and Machens, 2016; Hennequin et al., 2017; Shadlen and Newsome, 1994).

Pioneering models of balanced networks assumed sparse and random connectivity, which results in chaotic behavior (Denève and Machens, 2016; Renart et al., 2010; van Vreeswijk and Sompolinsky, 1996). Additional properties—including selective amplification of inputs, preferred activity states, and slow dynamics—can emerge in balanced networks with specific structure (Litwin-Kumar and Doiron, 2012; Murphy and Miller, 2009). Structured connectivity can amplify specific input patterns and generate runaway excitation, a problem that is prominent in recurrent memory networks (Brunel, 2016; Hopfield, 1982). This problem can be alleviated when excitatory and inhibitory gains are matched by co-tuning of excitatory and inhibitory synaptic inputs in individual neurons (Hennequin et al., 2012; Vogels et al., 2011). It has therefore been proposed that co-tuned connectivity is important to stabilize balanced memory networks (Hennequin et al., 2017; Rubin et al., 2017).

The systematic analysis of balanced networks is facilitated by the distinction between four types of excitatory-inhibitory balance (Denève and Machens, 2016; Hennequin et al., 2017): (1) Global balance described a network in which excitation and inhibition are balanced at the level of the population, but not necessarily in individual neurons. Hence, inhibition and excitation may be uncorrelated in individual neurons, but their ratio remains similar (balanced) when averaged across neurons or over

sufficiently long times. Global balance is the most general form of balance and occurs in all balanced networks. (2) Detailed balance requires that excitation and inhibition are balanced also in individual neurons. This occurs when excitatory and inhibitory inputs are co-tuned and therefore "balanced in coding space." This type of balance is also referred to as "high-dimensional balance" because it is maintained in most directions of coding space. (3) Tight balance means that excitatory and inhibitory inputs to individual neurons co-vary on fast timescales (milliseconds). As a consequence, synaptic currents in individual neurons remain balanced when the intensity of an external input fluctuates. (4) Precise balance refers to the coexistence of detailed and tight balance.

Strong excitation and inhibition consistent with a balanced state has been observed in multiple brain areas (Denève and Machens, 2016; Poo and Isaacson, 2009; Shu et al., 2003; Xue et al., 2014). Furthermore, in visual, auditory, and somatosensory cortices, excitatory and inhibitory synaptic currents can be co-tuned to basic stimulus features and co-vary in time (Anderson et al., 2000; Okun and Lampl, 2008; Oswald et al., 2006; Tan et al., 2004, 2011; Wehr and Zador, 2003; Wilent and Contreras, 2005). As these brain areas are topographically organized, co-tuning may be a result of local connectivity because nearby neurons are expected to receive similar sensory input. It remains unclear whether co-tuned connectivity represents a general principle also in less structured brain areas, such as autoassociative memory networks.

We addressed this question in the zebrafish homolog of olfactory cortex, the posterior zone of the dorsal telencephalon (Dp) (Mueller et al., 2011; Wullimann et al., 1996). Principal neurons in olfactory cortex receive stimulus-specific excitatory input from the output neurons of the olfactory bulb (OB), the mitral cells. In addition, neurons in piriform cortex receive recurrent excitatory input from other principal neurons and inhibitory input from local interneurons (Bekkers and Suzuki, 2013; Large et al., 2016; Stokes and Isaacson, 2010). Neither afferent projections nor the prominent recurrent connectivity within olfactory cortex exhibits an obvious topographic organization (Franks et al., 2011; Miyamichi et al., 2011; Sosulski et al., 2011). Consistent with this anatomical organization, odor-evoked activity in olfactory cortex is highly distributed (Bolding and Franks, 2017; Iurilli and Datta, 2017; Roland et al., 2017; Stettler and Axel, 2009; Wilson and Sullivan, 2011). Similar anatomical and functional observations were made in Dp (Blumhagen et al., 2011; Jacobson et al., 2018; Miyasaka et al., 2014; Yaksi et al., 2009), suggesting that olfactory cortex or Dp is initially an unstructured network that establishes autoassociative memories by experience-dependent plasticity of recurrent connections (Haberly, 2001; Hasselmo and Barkai, 1995; Wilson and Sullivan, 2011). Consistent with this hypothesis, olfactory discrimination training modified pattern separation and pattern completion in piriform cortex (Chapuis and Wilson, 2011), and rodents learned to distinguish optically evoked activity patterns in this brain area (Choe et al., 2015; Choi et al., 2011). In the piriform cortex of young rats, odors evoked prominent oscillatory synaptic currents (Poo and Isaacson, 2009). While excitatory inputs to individual neurons were tuned to odors, inhibition was reported to be global. Further results are, however, required to understand the precise organization of synaptic interactions in olfactory cortex and other memory networks.

We analyzed the functional organization of synaptic currents in Dp. Odor responses of Dp neurons frequently consist of a slow depolarization followed by a plateau phase that exceeds spike threshold in odor-dependent subsets of neurons (Blumhagen et al., 2011; Yaksi et al., 2009). Using whole-cell voltage clamp recordings we found that this membrane potential evolution reflects the transition of the network into a balanced state in posterior Dp (pDp). Neurons in pDp received strong, recurrent excitatory and inhibitory inputs that were co-tuned to different odors. Moreover, excitatory and inhibitory synaptic currents exhibited fast and almost synchronous oscillations that were phase-locked to the local field potential (LFP) oscillation in the OB. Synaptic currents converging onto individual neurons therefore co-varied across coding space and in time, implying that the balance between excitation and inhibition is precise. These results support theoretical models of precisely balanced networks and show that the functional synaptic organization in Dp supports efficient memory storage.

RESULTS

Basic Characterization of Neurons in Dp

To analyze the morphology, biophysical properties, and odor responses of individual neurons in the telencephalon of adult zebrafish, we performed whole-cell voltage clamp recordings (n = 247 neurons in 52 animals) in an *ex vivo* preparation of the intact brain and nose (Zhu et al., 2012). Positions of the recorded somata were mapped onto a 3D reference brain (Figures 1A–1D, Video S1). We focused primarily on a region referred to as posterior Dp (pDp; n = 120 recorded neurons; Figures 1A–1C) that is located posterior to the prominent furrow in the ventro-lateral pallium caudal to the anterior commissure (Figure 1C). pDp contains large, scattered somata and accounts for most of the volume of Dp as defined in the zebrafish brain atlas (Wullimann et al., 1996). In addition, we analyzed neurons in two adjacent areas of the pallium, anterior Dp (aDp) and the nucleus taeniae (NT). aDp (n = 55 recorded neurons) is located anterior to the furrow and separated from pDp by a population of densely packed somata. NT (n = 33 recorded neurons) is a superficial nucleus posterior to the furrow (Wullimann et al., 1996) and contains a high density of small somata. Additional recordings were performed from neurons at the interface between pDp and NT (n = 25) and in the furrow between aDp and NT (n = 14). Because these neurons could not be assigned unequivocally to pDp, aDp, or NT they were excluded from region-specific analyses.

Input resistances of neurons in pDp, aDp, and NT increased in the order pDp < aDp < NT (medians: 0.98 < 1.50 < 1.81 GΩ; Figure 1E; pDp: n = 89 neurons; aDp: n = 24; NT: n = 22; pDp versus aDp: p = 7.4e-5, pDp versus NT: p = 7.4e-9, aDp versus NT: p = 0.005; Wilcoxon rank-sum tests). Neurons at the interface between pDp and NT had intermediate input resistance (1.54 ± 0.65 GΩ; median ± SD; n = 8; data not shown). Light microscopic reconstructions of recorded neurons revealed that neuronal arbor size, as quantified by the equivalent spherical diameter of the convex hull, decreased in the order pDp > aDp > NT

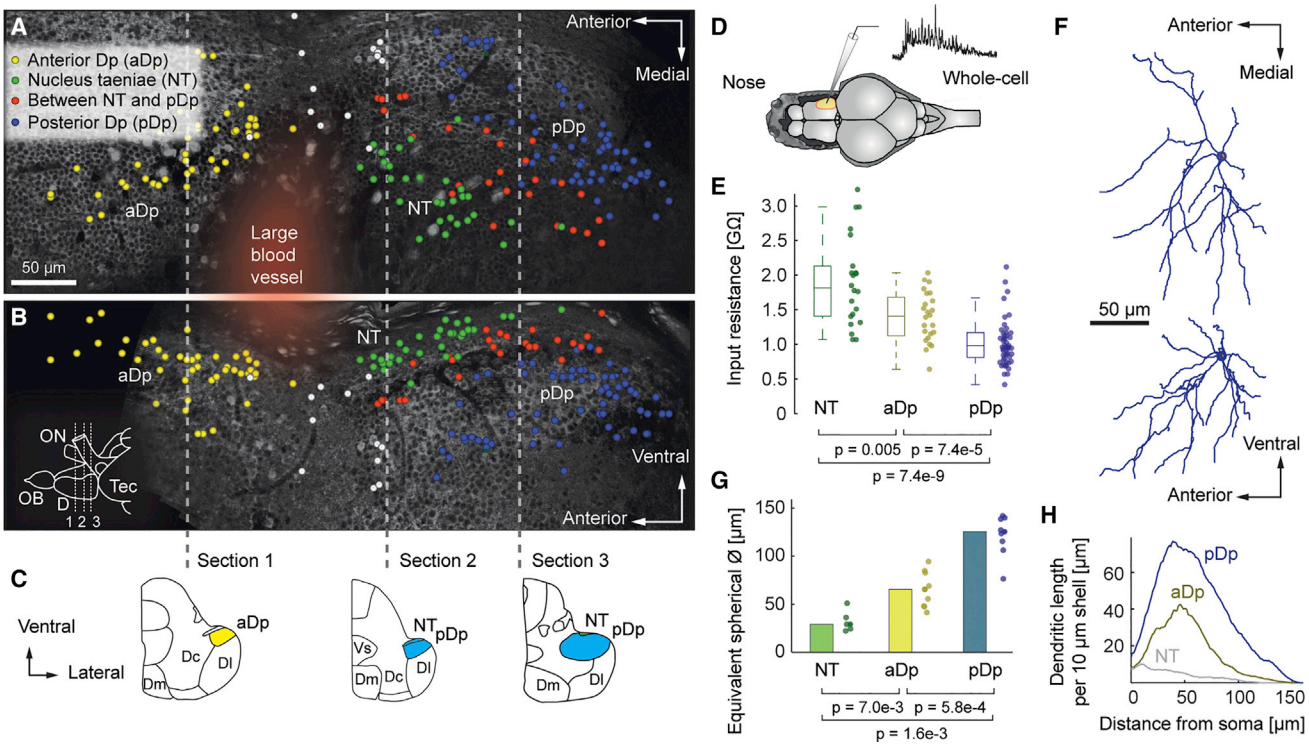

Figure 1. Anatomical and Biophysical Characterization of Neurons in Dp

(A) Mapping of somata onto an adult reference brain expressing GCaMP6f. Superficial telencephalic layers around Dp were extracted from a multiphoton image stack and projected into a horizontal plane (see also Video S1). Diffuse red color indicates the furrow below a large blood vessel (landmark). Dots show positions of somata from which odor responses were recorded in different fish (aDp, n = 46 neurons; NT, n = 33; pDp, n = 77; between NT and pDp, n = 25; white: between aDp and NT, n = 14).

(B) Surface projection of the reference brain onto a sagittal plane.

(C) Schematic coronal sections mapped onto approximate locations of the reference stack. Inset in (B) shows approximate locations of sections. ON: optic nerve, D: dorsal telencephalon, Tec: tectum.

(D) *Ex vivo* preparation (schematic; ventral view) and region targeted for recordings.

(E) Input resistance (pDp: n = 89 neurons; aDp: n = 24; NT: n = 22; all p values $\leq$ 0.005; Wilcoxon rank-sum test).

(F) Morphology of a pDp neuron in horizontal (top) and sagittal (bottom) projection. See also Figure S1 and Video S1.

(G) Equivalent spherical diameter of the convex hull of morphologically reconstructed neurons (pDp: n = 8 neurons; aDp: n = 9; NT: n = 5; all p values < 0.005; Wilcoxon rank-sum test).

(H) Sholl analysis, averaged across neurons. Drawings in (B) and (C) were modified from the zebrafish brain atlas (Wullimann et al., 1996).

(125 > 66 > 29 µm; Figure 1G; all p values < 0.005; Wilcoxon rank-sum test), consistent with input resistances. Neurons in pDp had multiple primary dendrites with extensive, space-filling higher-order branches (n = 8 reconstructions; Figures 1F and S1; Video S1). Neurons in aDp (n = 9) were also multipolar and branched, whereas neurons in NT (n = 5) had simpler morphologies. This observation was verified by Sholl analysis, which quantifies the amount of neurite as a function of the Euclidean distance from the soma. Neurite lengths of neurons in pDp and aDp peaked near 50 µm, whereas neurite lengths of NT neurons decreased continuously with distance from the soma (Figure 1H).

Synaptic Inputs to Neurons in pDp

To examine effects of sensory stimulation, we applied odors (amino acids [40 µM], bile acids [4 µM], or food extract) to the nose for $\geq$10 s. Multiphoton calcium imaging confirmed that odor-evoked activity patterns across mitral cells persisted and remained informative about stimulus identity throughout the stimulus period (Figure S2). In pDp, odor-evoked activity was most prominent during the first two seconds, but remained elevated for the full duration of the stimulus (Figure S3). Consistent with previous observations (Blumhagen et al., 2011; Yaksi et al., 2009), current clamp recordings showed that odor stimulation depolarized neurons in pDp (Figure 2C) with a magnitude depending on the neuron and odor. Sufficiently large depolarizations evoked action potentials with variable timing in repeated trials.

To analyze synaptic inputs to pDp neurons, we sequentially recorded excitatory and inhibitory postsynaptic currents (EPSCs and IPSCs) in voltage clamp by holding the membrane potential near the reversal potential of inhibitory (V_{hold} = −70 mV) and excitatory synaptic inputs (V_{hold} = 0 mV), respectively. In the absence of odor stimulation, pDp neurons received high rates of EPSCs and IPSCs that could not be separated into discrete events (Figures 2A and 2B).

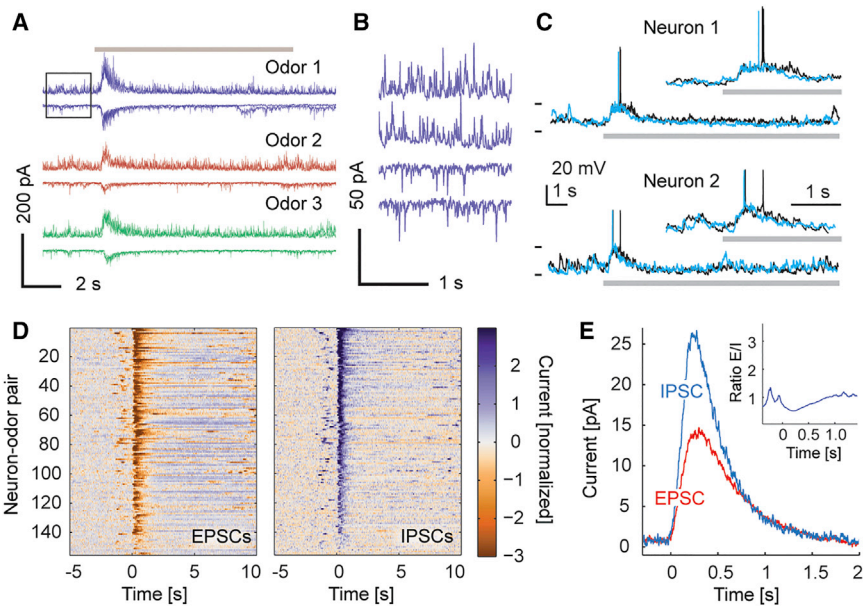

Figure 2. Odor-Evoked Input to pDp Neurons

(A) Examples of EPSCs (bottom; downward deflections) and IPSCs (top; upward deflections) evoked by three odors (colors) in a pDp neuron (overlay of two trials each). Grey bar indicates stimulus.

(B) Spontaneous currents at higher resolution (box in A).

(C) Current clamp recordings of odor responses from two pDp neurons (two trials each). Insets show response onset on expanded timescale. Ticks (left) indicate −70 and −40 mV. Grey bar indicates odor stimulation. Odor-evoked calcium signals are shown in Figures S2 and S3.

(D) Trial-averaged EPSCs (left) and IPSCs (right) for all n = 155 neuron-odor pairs in pDp (77 neurons), ordered by the mean evoked inhibitory current 0–1.5 s after stimulus onset. Each trace was centered by subtraction of the median prestimulus current and normalized to the prestimulus standard deviation. Transient currents observed occasionally ~2 s before stimulus onset (t = 0 s) were caused by small flow changes in the odor delivery system (STAR Methods).

(E) Average evoked inhibitory (blue) and excitatory (red) currents in pDp. Inset shows time course of the excitation:inhibition ratio.

In most pDp neurons, odor stimulation evoked large and transient compound EPSCs and IPSCs that decayed to a steady-state level after approximately two seconds (Figures 2D and 2E; recordings aligned to response onset, see STAR Methods). In subsets of neuron-odor pairs, persistent currents were observed after the initial transient (Figure 2D). Hence, odor stimulation evoked stimulus-dependent patterns of excitation and inhibition in pDp that were particularly prominent during the first two seconds.

Dp is expected to receive excitatory inputs from two main sources: long-range input from projection neurons in other brain areas, particularly in the OB (external input), and local input from other Dp neurons (recurrent input). To determine the relative contributions of these inputs, we injected the $GABA_A$ receptor agonist muscimol (5 mM in ACSF) into aDp, pDp, and NT (Figure 3A. Odor-evoked currents were compared to responses recorded in the absence of muscimol in different fish (control 1) and to responses of other neurons in the same fish prior to muscimol injection (control 2). Muscimol strongly reduced the input resistance of neurons in pDp (Figure 3B). Effects of muscimol on input resistances in aDp and NT were smaller but still substantial, indicating that neurons in pDp, aDp, and NT receive prominent inhibitory input (Figure 3B). Consistent with this conclusion, muscimol injections completely suppressed spontaneous and odor-evoked activity in pDp, aDp, and NT, as demonstrated by multiphoton calcium imaging (Figure 3C). No obvious attenuation of odor-evoked activity was observed in the OB, confirming that direct effects of muscimol remained local (Figure S4). Hence, muscimol injections isolated external synaptic inputs by silencing recurrent input.

Muscimol strongly decreased odor-evoked excitatory input to pDp neurons (Figures 3D and 3E; n = 15 neurons for muscimol, n = 72 for control 1, n = 6 for control 2). On average, the mean current during the first 1.5 s of the response was reduced to ~18% of control (Figure 3F; 13% ± 11% with respect to control 1, p = 3e-7; 19% ± 18% with respect to control 2, p = 7e-5; Wilcoxon rank-sum tests; mean ± SD). Moreover, oscillatory fluctuations of odor-evoked currents were diminished, but not completely abolished, by muscimol (Figures 3D and 3G). To test whether effects of muscimol may be mediated by presynaptic $GABA_B$ receptors on external inputs we also co-injected muscimol with the $GABA_B$ receptor antagonist SCH50911 (n = 10 neurons for muscimol + SCH50911, n = 5 neurons for control 3 in the same fish) (Liu et al., 2007; Yamauchi et al., 2000). SCH50911 did not antagonize effects of muscimol on mean EPSCs (Figures 3E–3G; 10% ± 11% of control 3, p = 6.7e-4; 13% ± 21% of control 1, p = 9.1e-7) and oscillatory fluctuations, indicating that presynaptic inhibition through $GABA_B$ receptors cannot account for effects of muscimol. Consistent with this conclusion, muscimol did not significantly affect excitatory input in aDp (see below). These results indicate that odor-evoked excitatory input to pDp neurons comes mainly from recurrent inputs.

To analyze odor tuning of synaptic inputs we used a procedure that takes trial-to-trial variability into account and makes no prior assumption about tuning curves. Mean EPSCs and IPSCs were quantified in response to three different odors, each of which was repeated multiple times (EPSCs: 3.4 ± 1.4 times; IPSCs: 3.2 ± 1.2 times; mean ± SD). For each neuron, we computed the variance of responses across trials and odors (Var_{pre}). We then subtracted the odor-specific means from the corresponding trials and re-calculated the variance (Var_{post}, Figure 4A). The relative difference $Var_{stim} = (Var_{pre} - Var_{post}) / Var_{pre}$ provides an initial estimate for the fraction of the variance across

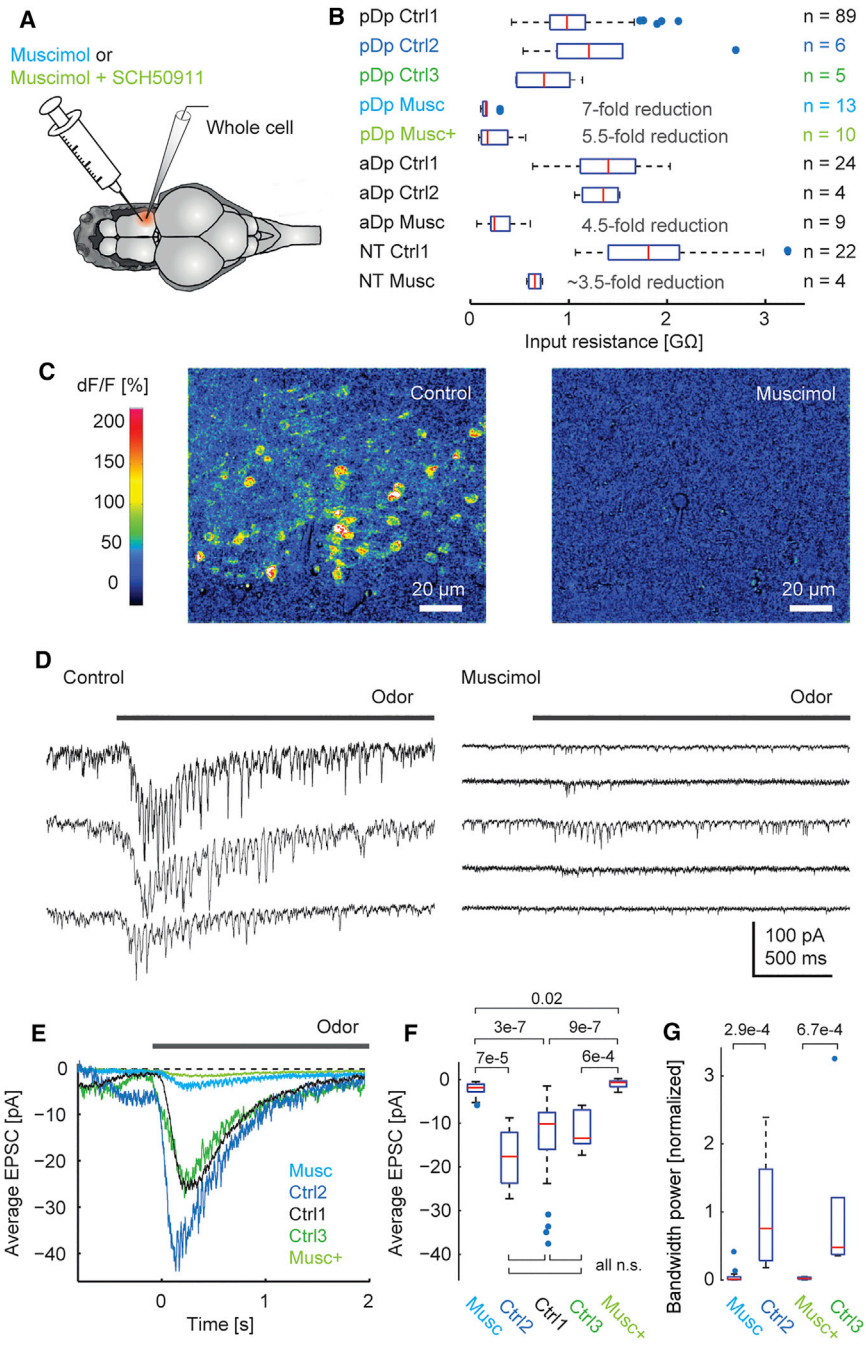

Figure 3. Effects of Local Silencing on Odor-Evoked Currents

(A) Muscimol injection: schematic.

(B) Effects of muscimol (Musc) and muscimol + SCH50911 (Musc+) on input resistance. Fold reduction indicates ratio of input resistances in control (Ctrl1) and muscimol conditions. Ctrl1: recordings in the absence of muscimol in different fish. Ctrl2: control recordings in fish that were later used for Musc application. Ctrl3: control recordings in fish that were later used for Musc+ application. Differences were statistically significant (Wilcoxon rank-sum test; all values for comparison to Ctrl1): pDp Musc: $p < 1e\text{-}9$; pDp Musc+: $p < 1e\text{-}6$; aDp Musc: $p < 1e\text{-}4$; NT Musc: $p < 1e\text{-}2$.

(C) Odor-evoked activity in pDp before and after Musc injection measured by multiphoton calcium imaging. See also Figure S4.

(D) Odor-evoked EPSCs under control conditions (left) and in the presence of Musc (right). Each trace is from a different pDp neuron.

(E) Time course of EPSCs averaged across neurons and odors.

(F) Mean current during the first 1.5 s of the response. Numbers of experiments as in (B). Mean current in Musc was significantly different from Ctrl1 (13% ± 11% of control; mean ± SD; $p = 3e\text{-}7$, Wilcoxon rank-sum test) and from Ctrl2 (19% ± 18%; $p = 7e\text{-}5$). Mean current in Musc+ was significantly different from Ctrl1 (13% ± 21%; $p = 9e\text{-}7$) and Ctrl3 (10% ± 11%; $p = 4e\text{-}4$).

(G) Maximum power (20–30 Hz) of EPSCs during the first 1.5 s of the response in Musc ($p = 2.9e\text{-}4$, comparison with Ctrl2; Wilcoxon rank-sum test) and Musc+ ($p = 6.7e\text{-}4$, comparison with Ctrl3).

all single-trial responses that can be explained by the odor stimulus. We then re-computed the fraction of the variance explained after shuffling stimulus labels between trials (Var_{chance}). The difference $\Delta Var = Var_{stim} - Var_{chance}$ thus provides an estimate of tuning, or discriminability, that takes trial-to-trial variability into account.

Var_{stim} was significantly larger than Var_{chance} for EPSCs and IPSCs. Hence, excitatory and inhibitory synaptic inputs were both tuned to odors. The difference ΔVar was large during the early phase of the response (0 – 1.5 s; Figure 4B; $p < 1e\text{-}6$ and $p < 1e\text{-}8$ for IPSCs and EPSCs, respectively; Wilcoxon rank-sum test) and smaller, but still significant, during the late phase (2 – 10 s; Figure 4C; $p < 1e\text{-}3$ and $p < 1e\text{-}2$). During the early phase, ΔVar of EPSCs (42%; Hodges–Lehmann estimator) was not or only slightly larger than ΔVar of IPSCs (36%; $p = 0.06$, Wilcoxon rank-sum test). Inhibitory synaptic input was therefore not or only slightly more broadly tuned than excitatory synaptic input. Similar results were obtained using more basic analyses of tuning curves that do not consider trial-to-trial variability (not shown). Hence, excitatory and inhibitory synaptic inputs to pDp exhibit a similar degree of tuning.

Odor Stimulation Induces a Balanced State in pDp

Mean odor-evoked excitatory and inhibitory currents in pDp were temporally symmetric (Figure 2E), raising the possibility that pDp enters a balanced state during an odor response. In a balanced state, the total synaptic conductance is substantial relative to the resting conductance and establishes a membrane potential near spike threshold (−37.2 ± 2.3 mV; mean ± SD;

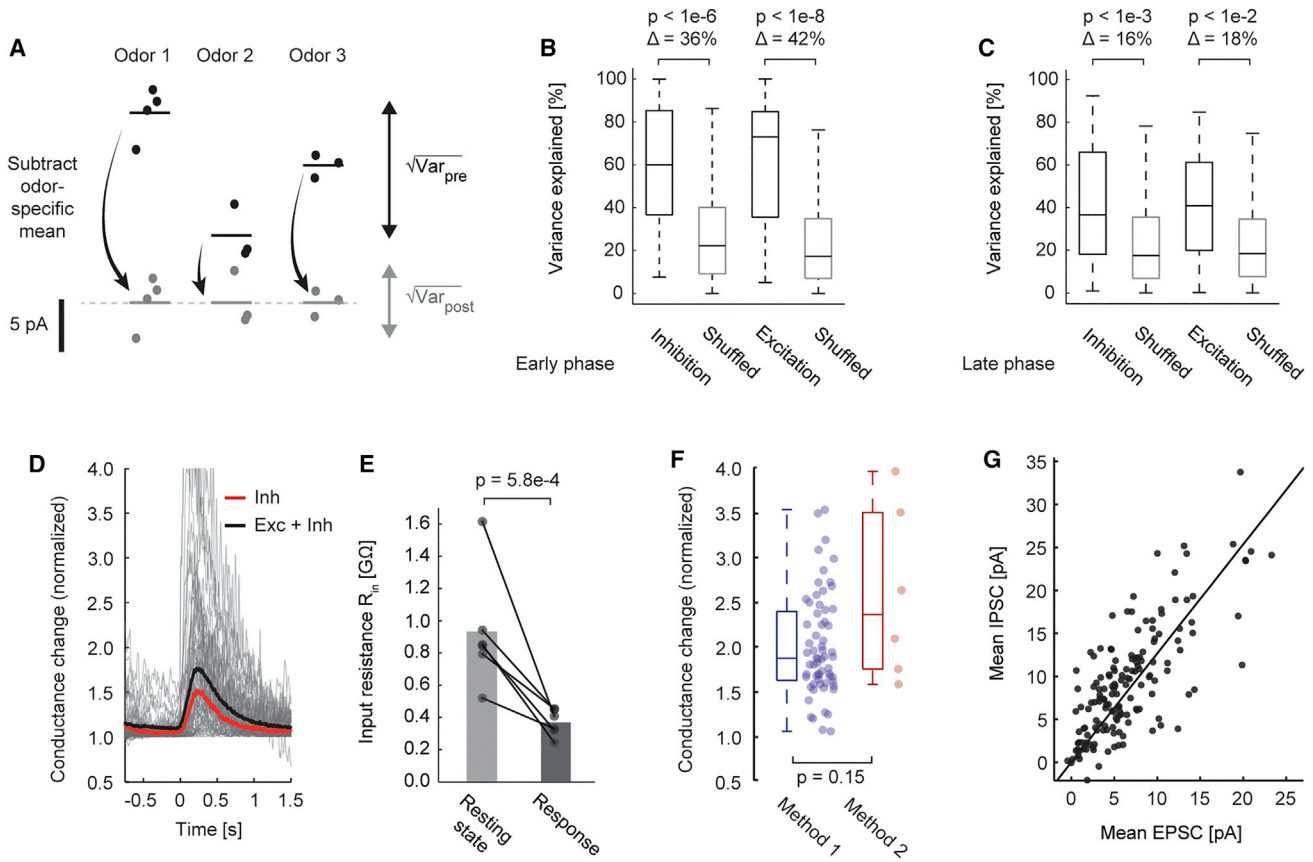

Figure 4. Tuning and Balance of Synaptic Currents in pDp

(A) Quantification of tuning: schematic illustration. The fraction of variance explained by tuning is $Var_{stim} = (Var_{pre} - Var_{post})/Var_{pre}$. In this example, $Var_{stim} = (30.3\ pA^2 - 4.0\ pA^2)/30.3\ pA^2 \approx 87\%$.

(B) Black: variance of EPSCs and IPSCs in pDp neurons explained by tuning (Var_{stim}). Currents were averaged over the first 1.5 s of the odor response. Gray: variability explained after shuffling of trial labels for each neuron (Var_{chance}; p < 1e-8 and p < 1e-6 for EPSCs and IPSCs, respectively; effect size 42% and 36%; Wilcoxon rank-sum test; n = 42 neurons).

(C) Variance explained by tuning after averaging currents 2–10 s after response onset (p < 1e-3 and p < 1e-2; 18% and 16%).

(D) Mean conductance of pDp neurons normalized to pre-stimulus baseline (t = 0: response onset). Gray: total conductance (inhibitory plus excitatory) of 155 individual neuron-odor pairs from 77 neurons (black: mean). Red: mean inhibitory conductance. See also Figure S5A.

(E) Input resistance of pDp before and during the first 1.5 s of odor stimulation, measured using test pulses (p = 5.8e-4; Wilcoxon signed-rank test; n = 6 neurons).

(F) Conductance change determined by recordings of synaptic currents (Method 1) and by test pulse injection (Method 2; p = 0.15, Wilcoxon rank-sum test).

(G) Relation between excitatory and inhibitory currents during the first 1.5 s of the odor response (n = 155 neuron-odor pairs from 77 neurons). Line shows a linear fit (slope: 1.26; $r = 0.73$, p < 1e-6). See also Figure S6.

n = 10 pDp neurons). To explore this possibility, we estimated the total conductance changes evoked by odor stimulation in individual neuron-odor pairs based on the recorded EPSCs and IPSCs. Conductance estimates were then normalized to the baseline conductance, which was derived from input resistance measurements (n = 89 neurons, Figure 1E). During the initial phase of the response, conductance increased 1.75-fold on average and > 4-fold during strong responses (Figure 4D). Most of the stimuli used in these experiments were individual amino acids, which activate glomeruli only in a restricted subregion of the OB (Friedrich and Korsching, 1997). In an additional set of experiments, we used food odors, which activate a larger number of glomeruli (Tabor et al., 2004), and determined the membrane conductance before and during the first 1.5 s of odor presentation by direct input resistance measurements using brief voltage pulses (50 ms, voltage step ΔV = −5 mV). In these experiments, the input resistance decreased 2.6- ± 1.0-fold during responses (mean ± SD; p = 5.8e-4, Wilcoxon signed-rank test; n = 6 neurons; Figure 4E), corresponding to a 2.6-fold increase in conductance (Figure 4F).

The observed conductance change does not directly reflect the ratio between the total synaptic conductance and the resting conductance for at least four reasons. First, the seal resistance contributes significantly to the measured input resistance (Figure S5A). Second, imperfect space clamp reduces synaptic currents in distal processes. Third, the resting conductance was measured without blockade of spontaneous activity. These three factors result in a systematic and possibly substantial underestimation of the true ratio between the synaptic and the resting conductance. A fourth factor is the K^+ channel blocker Cs^+ in

the pipette. To assess the influence of Cs^+, we recorded 17 additional neurons in pDp in the absence of Cs^+. As expected, the input resistance was significantly lower in the absence of Cs^+ (0.84 ± 0.27 GΩ; mean ± SD; with Cs^+: 1.05 ± 0.34 GΩ; n = 89 neurons; p = 0.029, Wilcoxon rank-sum test). The measured resistance depends on the resting conductance and on synaptic conductances activated by spontaneous activity. One extreme scenario is that spontaneous activity is negligible and the input resistance is determined by the resting conductance, which is incompletely blocked by Cs^+. The ratio between synaptic and resting conductance would thus be slightly overestimated (~20%). In another extreme scenario, the resting conductance is completely blocked by Cs^+, and the remaining conductance reflects synaptic input. The ratio between synaptic and resting conductance would thus be massively underestimated (~400%). We therefore conclude that the conductance of pDp neurons increases approximately two- to ten-fold during an odor response, with considerable variability between neuron-odor pairs. Hence, even in a conservative scenario, the membrane potential depends strongly on the ratio between excitatory and inhibitory synaptic inputs.

When mean odor-evoked EPSCs and IPSCs in pDp during the first 1.5 s of the odor response were pooled across neuron-odor pairs, excitatory and inhibitory synaptic responses were highly correlated (r = 0.73; p < 1e-6; Figure 4G; see also Figure S6), implying that excitation and inhibition were globally balanced. On average, IPSCs were 1.26 times larger than EPSCs. As a consequence, the reversal potential of the net synaptic conductance should establish a membrane potential near action potential threshold (−39 mV), consistent with current clamp recordings (Figure 2C; Yaksi et al., 2009). We therefore conclude that pDp enters a high-conductance balanced state during an odor response.

Because neurons in balanced networks operate close to their action potential threshold, balanced networks can follow fast input signals even when membrane time constants are long. In pDp, we frequently observed large oscillatory fluctuations of EPSCs and IPSCs at a frequency of ~25 Hz that are likely driven, directly or indirectly, by oscillatory activity in the OB (Blumhagen et al., 2011; Friedrich et al., 2004; Friedrich and Laurent, 2001). Consistent with this assumption, oscillatory currents were still observed in the presence of muscimol (Figure 3D) although their amplitude was strongly reduced (Figure 3G; p = 2.9e-4). These results imply that network activity in pDp can amplify inputs with an oscillation period (40 ± 2 ms, mean ± SD; n = 13 LFP recording sites in 3 fish) that is shorter than the membrane time constant in the resting state (55 ± 12 ms, mean ± SD; n = 56 neurons) and only ~2-fold longer than the time constant in the high-conductance state during an odor response (~21 ms). The pDp network therefore exhibits substantial temporal bandwidth during an odor response, further supporting the conclusion that pDp enters a balanced state.

Odor Responses in aDp Are Not Balanced

We next examined whether neurons in aDp also enter a balanced state during an odor response. In the absence of stimulation, aDp neurons received large and discrete EPSCs and IPSCs at low frequency. During stimulation, the rate of EPSCs and IPSCs increased but individual events were still distinguishable (Figures 5A–5C and S7; see also Figure 5G). Hence, aDp neurons received sparse synaptic inputs, contrary to the high-frequency input observed in pDp (Figure 2B).

EPSCs and IPSCs of aDp neurons showed significant odor tuning that was more pronounced at later response phases (Figures 5D and 5E). Mean odor-induced currents and conductance changes were substantially smaller than in pDp (Figure 5C). The total conductance increased, on average, less than 1.2-fold at its peak (not shown). Average EPSCs and IPSCs of aDp neurons during the first 1.5 s of an odor response were correlated across neuron-odor pairs (r = 0.57, p < 1e-6). The slope of a linear fit was 1.7, resulting in a combined synaptic reversal potential of −44 mV (Figure 5F, black). However, unlike in pDp, the average time course of odor-evoked EPSCs and IPSCs in aDp was not symmetric. While the mean EPSC remained almost constant, the mean IPSC decayed substantially during the 10 s of odor presentation (Figure 5C). As a consequence, the excitation:inhibition ratio changed approximately 10-fold (Figure 5C), implying that synaptic inputs were not balanced. Moreover, EPSCs and IPSCs in individual neuron-odor pairs often evolved differently (Figure 5B) and became uncorrelated at later response phases (r = 0.08, p = 0.39; Figure 5F, gray) when inputs were more informative about stimulus identity (Figures 5D and 5E). These results indicate that synaptic inputs to neurons in aDp do not support a balanced state.

Unlike in pDp, muscimol had only minor effects, if any, on spontaneous or odor-evoked EPSCs in aDp (Figures 5G–5K; n = 9 neurons). To quantify these observations, we analyzed short (5 – 10 ms) and discrete events representing individual EPSCs (Figures 5H–5K). In the presence of muscimol, the rate and temporal integral of these events was not significantly different from controls (Figures 5E–5H; p > 0.05; Wilcoxon rank-sum test), both during spontaneous activity and during odor responses. These results indicate that neurons in aDp are driven mainly by external input.

Detailed Balance in pDp

We next asked whether excitation and inhibition in pDp are balanced only at the population level (global balance, Figure 6A) or also in individual neurons (detailed balance, Figure 6B). In a network with detailed balance, EPSCs and IPSCs in individual neurons strictly co-vary in response to changing input, which implies correlated tuning curves of excitatory and inhibitory inputs to stimuli of different identity (“co-tuning”). In a globally balanced network without detailed balance, EPSCs and IPSCs in individual neurons are not co-tuned to stimulus identity, but correlations between EPSCs and IPSCs can still arise from two factors that we refer to as “stimulus strength” and “neuronal size.” First, correlated variations of EPSCs and IPSCs can occur when different stimuli generate different total amounts of input to the network (difference in stimulus strength). Second, correlations between EPSCs and IPSCs across a population occur when mean current amplitudes differ systematically between neurons, for example due to size differences (neuronal size) (Xue et al., 2014). The observed balance of EPSCs and IPSCs pooled over neurons and stimuli (Figure 4G) may therefore reflect a combination of three factors: stimulus strength, neuronal size, and

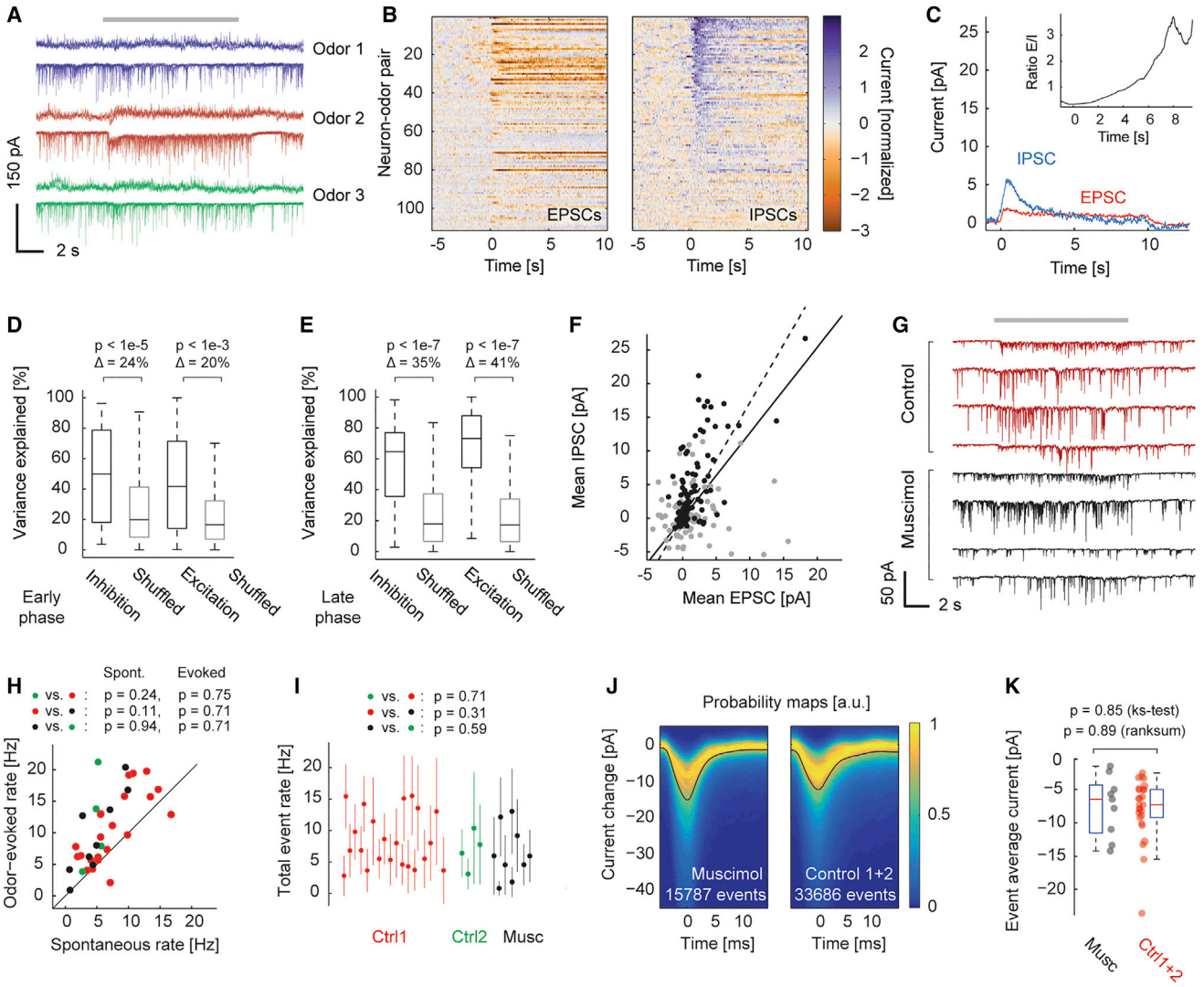

Figure 5. Synaptic Currents in aDp Are Not Balanced

(A) EPSCs (bottom; downward deflections) and IPSCs (top; upward deflections) evoked by three odors in an aDp neuron. Overlay of two trials each; gray bar indicates stimulus.

(B) Trial-averaged EPSCs and IPSCs in aDp (n = 111 neuron-odor pairs in 46 neurons), ordered by the average IPSC amplitude 0–1.5 s after stimulus onset. Each trace was normalized by the pre-stimulus standard deviation after subtraction of the median pre-stimulus current.

(C) Average odor-evoked EPSC and IPSC in aDp. Axis scaled as in Fig. 2D.

(D) Variance explained by tuning in aDp neurons during the first 1.5 s of the odor response. Gray: same after shuffling of trial labels ($p < 1e\text{-}3$ and $p < 1e\text{-}5$ for EPSCs and IPSCs, respectively; effect size 20% and 24%; Wilcoxon rank-sum test; n = 26 neurons).

(E) Same as in (D) 2–10 s after stimulus onset ($p < 1e\text{-}7$ and $p < 1e\text{-}7$ for EPSCs and IPSCs; effect size 41% and 35%).

(F) Relation between excitatory and inhibitory currents in aDp neurons (black; 0–1.5 s). Dashed line is a linear fit (slope: 1.7; $r = 0.57$, $p < 1e\text{-}6$). The same relation is also plotted for a later time window of the same duration (gray; 8.5–10 s; $r = 0.08$, $p = 0.39$). The continuous line is the linear fit to data from pDp (Fig. 4G).

(G) EPSCs during odor stimulation (bar) in aDp under control conditions and in the presence of muscimol. Each trace is from a different neuron. See also Figure S7.

(H) Rate of automatically detected EPSC events in the absence (x axis) and presence (y axis) of an odor stimulus ($p > 0.10$ for all comparisons; Wilcoxon rank-sum test). Each data point represents one neuron. Muscimol (black): n = 9 neurons from 4 fish; Ctrl1 (red; neurons from other fish): n = 22 from 8 fish; Ctrl2: (green; neurons from the same fish recorded before muscimol injection): n = 4 from 3 fish.

(I) Same as (H) but rates averaged over the total recording time (muscimol: 17,692 events; Ctrl1: 23,177 events; Ctrl2: 8,719 events). Whiskers indicate the standard deviation of the rate for a given neuron when evaluated over a moving 1-s window.

(J) Event-triggered EPSC probability for the muscimol condition (n = 9 neurons from 4 fish) and control (right; n = 26 from 11 fish; Ctrl1 and Ctrl2 combined). Black line indicates median along the y axis.

(K) Mean currents in a 5-ms window around events, averaged separately for each neuron.

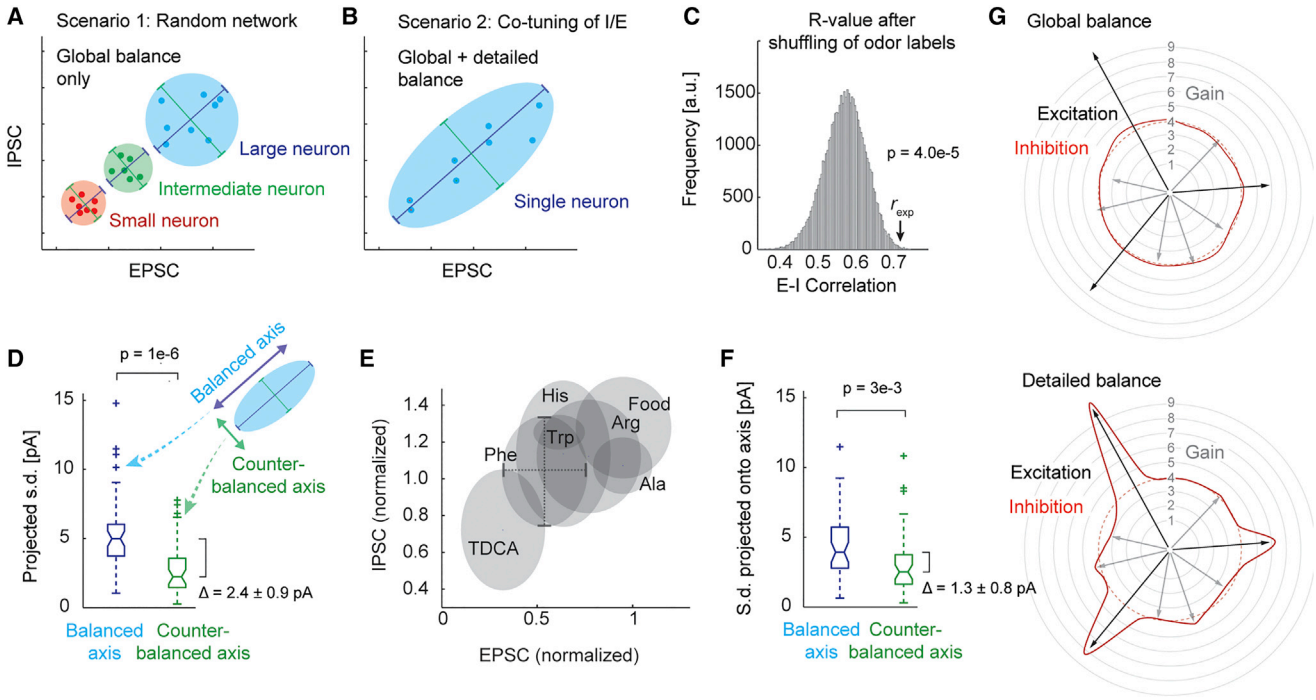

Figure 6. Detailed Synaptic Balance in pDp

(A) Schematic illustration of correlated EPSCs and IPSCs arising from global balance alone. Even though currents are uncorrelated in individual neurons, correlations may be created by systematic differences between neurons.

(B) Detailed balance, in contrast, implies correlations between currents also in individual neurons (see also Figure S5B).

(C) Distribution of Pearson correlation coefficients between EPSCs and IPSCs after shuffling stimulus labels for each neuron (mean ± SD: 0.57 ± 0.05). Given this distribution, the probability that the experimentally determined value (r_{exp} = 0.73) is observed by chance is p = 4e-5.

(D) Standard deviation of currents across stimuli projected onto the balanced axis and onto the orthogonal (counter-balanced) axis for individual neurons (p = 1e-6; Wilcoxon signed-rank test).

(E) Normalized excitatory and inhibitory currents evoked by different odors. Centroids represent means, while x and y axes of the ellipses indicate standard deviations across neurons (illustrated for Phe).

(F) Standard deviation of currents projected onto the balanced and counter-balanced axes as in (D) but after compensating for different "stimulus strengths" (p = 3e-3; Wilcoxon signed-rank test).

(G) Consequences of global and detailed balance in an autoassociative recurrent network. Radial axis indicates excitatory (arrows) and inhibitory (red contour) gain in different directions of coding space. Top: network with broadly tuned inhibition, as expected in global balance, but amplification of excitation along specific directions (long arrows), as established after learning. Inhibition cannot stabilize excitation in all directions. Bottom: co-tuning of excitation and inhibition (detailed balance) stabilizes activity in all directions.

co-tuning to stimuli of different identity (detailed balance). In a network with detailed balance, excitation and inhibition are correlated even in the absence of variations in stimulus strength and neuronal size. We therefore examined whether co-tuning persists after compensating for variations in stimulus strength and neuronal size.

We first shuffled odor labels of mean EPSCs and/or mean IPSCs recorded in the same neurons. This procedure independently randomizes tuning curves of excitatory and/or inhibitory synaptic inputs in each neuron but maintains variations in EPSCs and IPSCs between neurons. After shuffling, correlations between EPSCs and IPSCs across the population were significantly lower (0.57 ± 0.05 versus 0.73; mean ± SD; probability that a value of 0.73 is observed by chance: p = 4e-5; Figure 6C). Hence, correlations between EPSCs and IPSCs in individual neurons depend at least partially on their tuning. The correlation remaining after shuffling may reflect systematic differences in neuronal size. Consistent with this hypothesis, the total synaptic input and the inverse of the input resistance were significantly correlated (Figure S5B; r = 0.64; p = 4.6e-5).

To analyze co-variations of EPSCs and IPSCs more directly in individual neurons, we examined odor-evoked currents in a two-dimensional space representing mean EPSC and IPSC amplitudes (Figures 6A, 6B, and 6D, inset). We then projected odor responses onto two axes within this space. The first ("balanced") axis was chosen to be the direction of positively correlated variability in the population data (Figure 4G; "direction of balance"). The second ("counter-balanced") axis was orthogonal to the first, thus representing negatively correlated variability (Figures 6A, 6B, and 6D). If EPSCs and IPSCs recorded in the same neurons were uncorrelated, the variance along the two axes should, on average, be equal. However, we found that the variability along the balanced axis, as quantified by the square root of the variance, was significantly larger (ratio of medians 2.24; difference Δ = 2.41 ± 0.88 pA, pseudomedian ± 95% confidence intervals; p = 1e-6; Wilcoxon signed-rank test; Figure 6D). EPSCs and

IPSCs were therefore positively correlated even in individual neurons, implying that the observed co-variation between EPSCs and IPSCs cannot be fully explained by neuronal size.

The positive correlation of EPSCs and IPSCs in individual neurons could reflect variations in stimulus strength, co-tuning of synaptic inputs to odor identity, or both. To determine the stimulus strength of each odor while taking into account differences in neuronal size, we approximated the responses of all neurons i to all stimuli j by the product $s_j \cdot n_i$, where s_j is the stimulus strength of stimulus j and n_i is the neuronal size of neuron i, and jointly fitted s_j and n_i for all stimulus-neuron pairs. We then normalized responses of each neuron to neuronal size and averaged responses to the same odors across neurons to estimate stimulus strengths. Excitatory and inhibitory stimulus strengths differed between odors. Both increased approximately with the number of glomeruli activated by each odor (Friedrich and Korsching, 1997; Tabor et al., 2004) and showed a strong tendency to be correlated ($r = 0.71$; $p = 0.07$; Figure 6E; $n = 7$ stimuli). Differences in stimulus strength between odors are therefore likely to contribute to the correlation between excitatory and inhibitory synaptic currents observed in our experiments.

To compensate for both stimulus strength and neuronal size, we then normalized responses to stimulus strength and analyzed the variance of synaptic currents in individual neurons along the balanced and counter-balanced axes as before (Figure 6D). The variance along the balanced axis was still significantly larger than the variance along the unbalanced axis (ratio of medians 1.56; difference $\Delta = 1.32 \pm 0.84$ pA; pseudomedian ± 95% confidence intervals; $p = 0.0030$; Wilcoxon signed-rank test; Figure 6F). Hence, co-tuning of excitatory and inhibitory synaptic inputs with respect to odor identity was preserved after removing other sources of variability. Synaptic currents in pDp therefore exhibit a detailed balance during odor responses.

Tight Balance in pDp

To examine whether synaptic currents in pDp are also balanced in time, we further analyzed their dynamics. In current clamp recordings of odor responses, Dp neurons often showed an initial ramp-like depolarization, ~400 ms in duration, that was followed by a plateau (Figure 2C; Blumhagen et al., 2011; Yaksi et al., 2009). Action potentials were rare during the initial ramp but occurred when the plateau exceeded spike threshold. To examine the underlying synaptic currents, we normalized EPSCs and IPSCs during the first 1.2 s of the response to their maxima and analyzed their evolution in a two-dimensional phase plot (Figure 7A). Most trajectories described narrow ellipses along the diagonal, showing that excitatory and inhibitory synaptic inputs co-evolved in individual neurons. On average, excitation and inhibition increased in parallel during the first ~400 ms. Thereafter, inhibition decreased slightly faster than excitation, resulting in a small shift of the ratio in favor of excitation.

To verify these results we performed voltage-clamp recordings at different holding potentials with the cation channel blocker QX-314 in the pipette. Recordings at the reversal potentials for inhibitory and excitatory currents (−70 mV and 0 mV, respectively) confirmed that the overall time courses of IPSCs and EPSCs were similar but IPSCs evolved slightly faster (Figure 7B). Recordings of mixed synaptic currents at intermediate holding potentials (−35 mV) showed that the relative contribution of inhibitory currents was largest during the initial phase, while the relative contribution of excitatory currents peaked during later phases (> 400 ms; Figure 7C). Together, these data show that the balance between excitation and inhibition shifts slightly toward excitation at later response phases, which is likely to contribute to the delayed generation of action potentials (Blumhagen et al., 2011). However, because the magnitude of this shift was small, the balance between excitatory and inhibitory synaptic responses did not change substantially.

We then examined whether pDp enters a tightly balanced state, which usually refers to a balance of synaptic currents on a millisecond timescale (Denève and Machens, 2016; Hennequin et al., 2017). Tight balance would ideally be examined by simultaneous recordings of EPSCs and IPSCs from the same neurons, but this is technically not feasible. We therefore took advantage of the oscillatory temporal structure of EPSCs and IPSCs. Simultaneous voltage clamp recordings in pDp and LFP recordings in the OB showed that oscillatory EPSCs and IPSCs were tightly phase-locked to the odor-evoked LFP oscillation in the OB (Figures 7D–7F), confirming that the oscillatory temporal structure of synaptic activity in pDp is likely to originate in the OB. Moreover, the high correlations allowed us to use the LFP oscillation as a temporal reference in order to determine the relative timing of oscillatory EPSCs and IPSCs in pDp.

Cross-correlation functions between EPSCs or IPSCs and the LFP for individual neurons (Figure 7G) showed that EPSC oscillations slightly preceded IPSC oscillations (Figure 7H). Similar observations were made in all individual neurons (Figure 7I). On average, the time shift between EPSCs and IPSCs was 3.0 ± 0.3 ms (mean ± SEM), which is short relative to the period of the oscillation (~40 ms) and relative to the membrane time constant of neurons in pDp (55 ± 12 ms in the absence of odor stimulation; mean ± SD; $n = 56$ neurons). As a consequence, effects of EPSCs and IPSCs on the membrane potential neutralize each other with high efficiency. Consistent with this conclusion, previous current clamp recordings showed only small oscillatory fluctuations in the membrane potential of Dp neurons (Blumhagen et al., 2011). These results provide direct evidence that synaptic currents in pDp are tightly balanced in time.

DISCUSSION

We obtained direct biophysical evidence for a state of precise synaptic balance in pDp that emerges during odor stimulation and defines a reversal potential near spike threshold. Action potentials thus depend on variations in the balance between excitation and inhibition in individual neurons, which depend on external inputs and network connectivity. Excitatory and inhibitory synaptic currents in individual neurons were co-tuned in odor space and highly correlated on slow and fast timescales. This precise synaptic balance requires coordinated connectivity to match excitatory and inhibitory inputs to individual neurons. Synaptic connectivity therefore exhibits functional specificity despite the absence of an obvious spatial organization. Co-tuning can stabilize specific activity patterns in recurrent networks and thereby support autoassociative memory. However, unlike

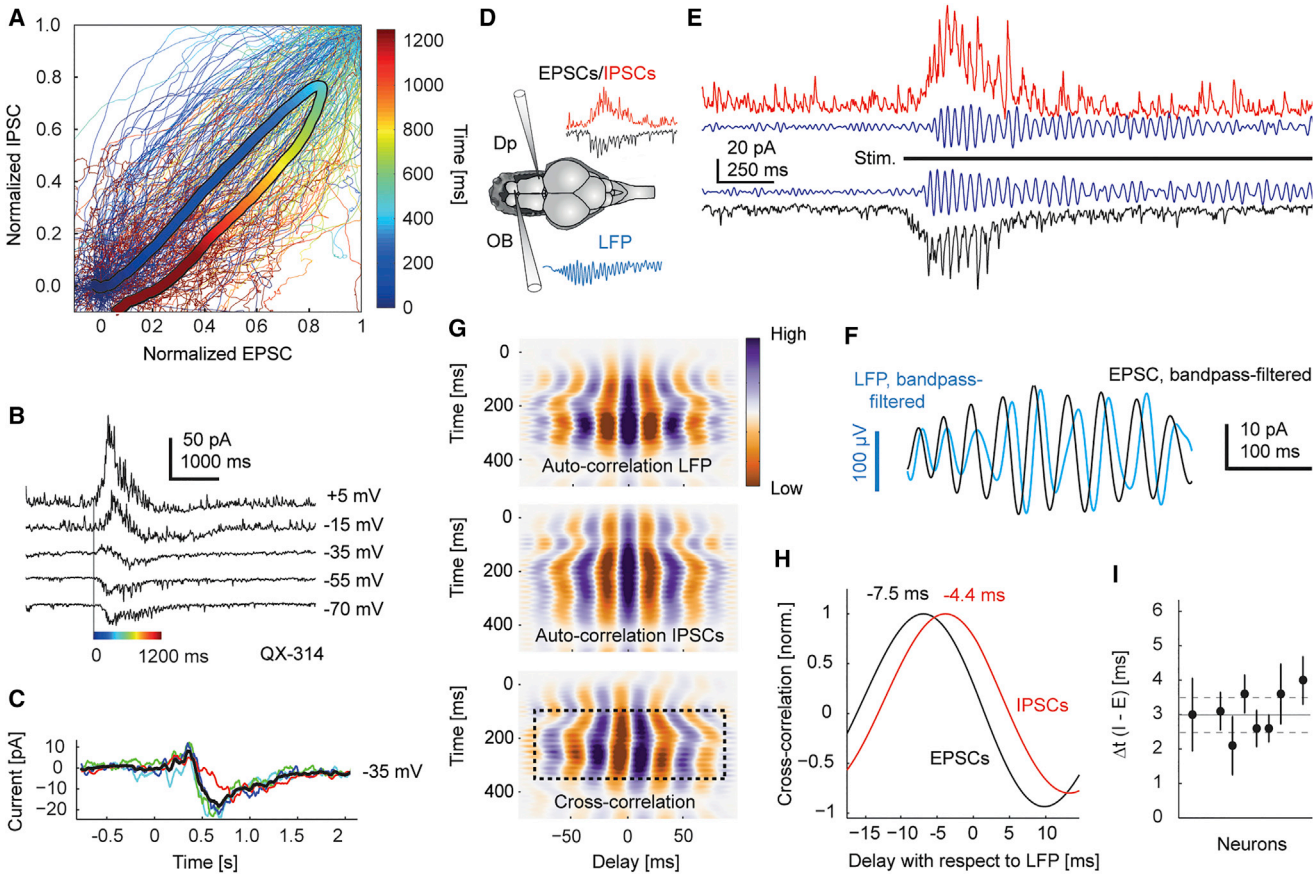

Figure 7. Relative Timing of Excitatory and Inhibitory Input Currents in pDp

(A) Phase plot of excitatory and inhibitory currents during the first 1.2 s of the odor response normalized to the maxima of EPSCs and IPSCs for each neuron-odor pair (n = 155 from 77 neurons). Time is color-coded. Thick line shows average over neurons.

(B) Odor-evoked currents in a pDp neuron held at different holding potentials with QX-314 in the recording pipette. Color scale indicates time as in (A).

(C) Currents recorded from four neurons with QX-314 in the pipette at an intermediate holding potential (−35 mV; black: average).

(D) Configuration of recordings.

(E) Simultaneous recordings of currents in a pDp neuron (red: IPSCs; black: EPSCs) and the LFP in the OB (blue; 15–40 Hz).

(F) Overlay of bandpass-filtered EPSC (black) and LFP (blue) recorded simultaneously during a response.

(G) Autocorrelograms of a typical LFP (top) and IPSC (middle) after response onset (t = 0). Bottom: cross-correlogram between LFP and IPSC.

(H) Cross-correlation functions between LFP and synaptic currents in an example neuron, averaged around the peak of the oscillation (box in G). Time shifts of the peak relative to the LFP in the OB are indicated. Inhibition is delayed relative to excitation by 3.1 ms.

(I) Delay between inhibition and excitation for n = 8 neurons. Whiskers indicate SEM of delays with respect to the LFP for single neurons.

classical attractor networks, balanced state networks can operate on fast timescales. pDp may therefore function as an autoassociative network that allows for the fast classification of learned inputs.

Synaptic Balance in Dp

The homology between Dp and piriform cortex (Mueller et al., 2011) is paralleled by functional similarities, including the absence of an obvious topography and pronounced mixture suppression of odor responses (Franks et al., 2011; Iurilli and Datta, 2017; Jacobson et al., 2018; Miyasaka et al., 2014; Roland et al., 2017; Stettler and Axel, 2009; Yaksi et al., 2009). We found that pDp neurons receive strong recurrent input and weaker input from external sources, as observed in piriform neurons (Haberly, 2001; Poo and Isaacson, 2011; Wilson and Sullivan, 2011), while aDp neurons received input primarily from external sources. These findings strengthen the notion that pDp, which comprises most of Dp, is closely related to piriform cortex, while the relationship between aDp and mammalian olfactory cortex remains to be clarified.

Odors evoked large EPSCs and IPSCs in pDp that followed similar time courses (Figure 2D) and were correlated across neuron-odor pairs. The combined reversal potential was close to action potential threshold, consistent with observations in current clamp (Yaksi et al., 2009). Hence, odor-evoked activity in pDp shows the hallmarks of a balanced state. Neurons in aDp, in contrast, received sparse EPSCs and IPSCs that followed different time courses during an odor response, implying that synaptic inputs are not balanced. Hence, pDp is functionally distinct from other telencephalic targets of the OB.

Large odor-evoked EPSCs and IPSCs consistent with a balanced state have also been observed in the piriform cortex of anesthetized rats (Poo and Isaacson, 2009). EPSCs were odor-selective, whereas IPSCs were reported to be untuned (Poo and Isaacson, 2009). In pDp, in contrast, inhibition and excitation were co-tuned. These different observations may reflect differences in circuit architecture or differences in experimental variables such as odor concentration. Moreover, as piriform neurons were recorded in young animals, co-tuned connectivity may be established later in development by an experience-dependent plasticity process. Consistent with this possibility, postnatal activity-dependent development of co-tuned inhibition has been described in the auditory cortex of rats (Dorrn et al., 2010; but see also Sun et al., 2010).

Co-tuned EPSCs and IPSCs consistent with a balanced state have also been observed in visual, auditory, and somatosensory cortices during sensory stimulation (Anderson et al., 2000; Okun and Lampl, 2008; Tan et al., 2004, 2011; Wehr and Zador, 2003; Wilent and Contreras, 2005). In these brain areas, co-tuning may arise as a consequence of a topographic organization that favors connectivity between neurons with similar tuning. Our results demonstrate that co-tuning can also occur in a non-topographic network that is likely to function as an autoassociative memory system. Co-tuning can, for example, arise when monosynaptic excitatory output and disynaptic feed-forward inhibition originating from the same principal neurons converge onto the same targets, which has been observed anatomically in entorhinal cortex (Schmidt et al., 2017). Co-tuning may therefore be a functional motif of multiple circuits (Hennequin et al., 2017).

Co-tuning implies that individual neurons co-select excitatory and inhibitory inputs based on their functional properties, presumably by coordinated and activity-dependent modifications of excitatory and inhibitory synapses (Chiu et al., 2018; D'amour and Froemke, 2015; Froemke, 2015). Computational studies demonstrated that synaptic plasticity rules consistent with this hypothesis can indeed establish co-tuned connectivity in network models (Hennequin et al., 2017; Vogels et al., 2011). Our observations therefore support the notion that neural circuits are refined by complex plasticity processes including the activity-dependent modification of inhibitory synapses.

Dynamics of Synaptic Odor Responses

After stimulus onset, EPSCs and IPSCs in pDp both increased for approximately 400 ms and thereafter decreased before approaching a stable level. Hence, large synaptic conductances supporting a balanced state developed gradually and were transient, despite persistent input from the OB. The mechanisms underlying this dynamics of balanced synaptic currents during an odor response may involve short-term synaptic plasticity but remain to be analyzed in detail.

On faster timescales, odor-evoked EPSCs and IPSCs exhibited prominent oscillatory fluctuations that were most likely transmitted from the OB and amplified in pDp. Similar oscillatory EPSCs and IPSCs were observed in piriform cortex (Poo and Isaacson, 2009). Because the time shift was small, EPSCs and IPSCs largely antagonize each other and should result in modulations of the membrane potential that are small. Indeed, oscillatory membrane potential and firing rate modulations in Dp were minimal when oscillatory synchronization in the OB was modulated over a broad range (Blumhagen et al., 2011). Nevertheless, the timing of action potentials and synaptic currents followed oscillatory activity in the OB, consistent with the high temporal bandwidth of a tightly balanced network. Tight balance in pDp therefore stabilizes firing rates against temporal fluctuations without an obvious loss in bandwidth.

Previous studies showed that firing rate responses of Dp neurons are insensitive to synchrony in their inputs and often exhibit long latencies (Blumhagen et al., 2011). As a consequence, responses of Dp neurons are biased toward non-synchronized inputs during later phases, which are particularly informative about precise odor identity (Friedrich et al., 2004). The slow dynamics of synaptic balance in pDp attenuates responses during the initial response phase, while tight balance reduces the impact of synchrony on firing rates. Hence, the dynamics of synaptic balance in pDp is likely to support the readout of odor identity information in pDp.

Computational Consequences of Precise Balance

Balanced networks produce specific responses to external inputs that depend on the precise pattern and temporal structure of these inputs. When the balance is only global, uncorrelated excitation and inhibition is prone to saturate the dynamic range of a subset of neurons. In precisely balanced networks, in contrast, excitation and inhibition are matched in individual neurons even when the overall variance of synaptic currents is large. Precisely balanced networks can therefore generate stable responses to a broader set of inputs.

Tight balance reduces uncorrelated fluctuations in excitatory and inhibitory inputs, which would inject noise into the network (Boerlin et al., 2013; Denève and Machens, 2016; Hennequin et al., 2017). As a consequence, tight balance can make action potentials more informative, generate robustness of population activity against temporal fluctuations, and support auto-encoding (Denève et al., 2017). Detailed balance, on the other hand, stabilizes population activity against variations in the amplification of different inputs (Figure 6G), which depends on the match between an input pattern and the pattern of recurrent excitatory connections. Large variations in amplification can occur in autoassociative networks because strengthening of specific excitatory connectivity enhances amplification along selected directions in coding space. Detailed balance prevents instabilities that may arise from non-uniform amplification because it matches excitation and inhibition in different directions of coding space. Hence, detailed balance may enhance associative memory storage in pDp (Haberly, 2001; Wilson and Sullivan, 2011).

Previous models of piriform cortex are related to autoassociative memory networks with attractor dynamics (Wilson and Sullivan, 2011), which act as classifiers and working memory devices because they map inputs onto stable network states (Brunel, 2016; Chapeton et al., 2012; Hopfield, 1982). Some fundamental features of these models, including pattern separation and completion, are consistent with experimental observations (Wilson and Sullivan, 2011) but persistent activity does not appear to be prominent in piriform cortex or Dp (Bolding and Franks, 2017; Iurilli and Datta, 2017; Miura et al., 2012). It may thus be interesting to consider potential consequences of

a balanced state in network models related to olfactory cortex. One feature of balanced networks is that they are well suited for intensity-invariant computations because they are insensitive to the mean of external inputs. This property may support the selective readout of odor identity information in pDp (Bolding and Franks, 2017). Second, synaptic balance supports memory and classification operations because it enhances the ability of recurrent networks to amplify specific input patterns (Hennequin et al., 2012; Murphy and Miller, 2009). Third, balanced synaptic activity suppresses noise arising within the network (Rubin et al., 2017). Fourth, unlike classical attractor networks, balanced networks have a high temporal bandwidth and can switch rapidly between different output patterns. An autoassociative memory network entering a balanced state can thus act as an experience-dependent classifier with a high dynamic range but without working memory (Murphy and Miller, 2009; Vogels et al., 2011), which appears advantageous for sensory processing and predictive processing. The performance of such classifiers is greatly enhanced by co-tuning of excitation and inhibition (Hennequin et al., 2012, 2017), and connectivity consistent with this assumption emerged after training of a balanced network on a pattern discrimination task (Rubin et al., 2017). The precise balance of synaptic activity in pDp may therefore support functions related to fast autoassociative memory and pattern classification.

STAR★METHODS

Detailed methods are provided in the online version of this paper and include the following:

- KEY RESOURCES TABLE
- CONTACT FOR REAGENT AND RESOURCE SHARING
- EXPERIMENTAL MODEL AND SUBJECT DETAILS
- METHOD DETAILS
  - Surgery for *ex vivo* experiments
  - Odor application
  - Electrophysiology
  - Mapping of neuron positions onto a reference stack
  - Temporal alignment of voltage clamp recordings
  - Analysis of biophysical properties of neurons
  - Tracing of neurites
  - Muscimol and SCH50911 injection
  - Calcium imaging experiments
- QUANTIFICATION AND STATISTICAL ANALYSIS
  - Co-tuning analysis for pDp neurons
  - Cross-correlation of simultaneous recordings
  - Detection of events for aDp recordings
  - Power analysis in the 20-30 Hz band
  - Analysis of calcium imaging experiments
  - Decorrelation and stability analysis in the OB
  - Statistical analysis
- DATA AND SOFTWARE AVAILABILITY

SUPPLEMENTAL INFORMATION

Supplemental Information includes seven figures and two videos and can be found with this article online at https://doi.org/10.1016/j.neuron.2018.09.013.

ACKNOWLEDGMENTS

We thank Claire Meissner-Bernard, Thomas Frank, Yael Bitterman, and Georg Keller for comments on the manuscript; Katharina Behr for support on electrophysiology; and the Friedrich group for stimulating discussions. This work was supported by the Novartis Research Foundation, by the Swiss National Science Foundation (SNF; 310030B_152833/1), by the European Research Council (ERC) under the European Union's Horizon 2020 research and innovation program (grant agreement No 742576), and by a fellowship from the Boehringer Ingelheim Fonds to P.R.

AUTHOR CONTRIBUTIONS

P.R. designed the study, performed the experiments, analyzed data, and wrote the manuscript. R.W.F. designed the study, made minor contributions to the analysis of the data, and wrote the manuscript.

DECLARATION OF INTERESTS

The authors declare no competing interests.

Received: March 28, 2018
Revised: July 4, 2018
Accepted: September 6, 2018
Published: October 11, 2018

REFERENCES

Ahrens, M.B., Orger, M.B., Robson, D.N., Li, J.M., and Keller, P.J. (2013). Whole-brain functional imaging at cellular resolution using light-sheet microscopy. Nat. Methods *10*, 413–420.

Anderson, J.S., Carandini, M., and Ferster, D. (2000). Orientation tuning of input conductance, excitation, and inhibition in cat primary visual cortex. J. Neurophysiol. *84*, 909–926.

Bekkers, J.M., and Suzuki, N. (2013). Neurons and circuits for odor processing in the piriform cortex. Trends Neurosci. *36*, 429–438.

Berens, P., Freeman, J., Deneux, T., Chenkov, N., McColgan, T., Speiser, A., Macke, J.H., Turaga, S.C., Mineault, P., Rupprecht, P., et al. (2018). Community-based benchmarking improves spike rate inference from two-photon calcium imaging data. PLoS Comput. Biol. *14*, e1006157.

Blumhagen, F., Zhu, P., Shum, J., Schärer, Y.P., Yaksi, E., Deisseroth, K., and Friedrich, R.W. (2011). Neuronal filtering of multiplexed odour representations. Nature *479*, 493–498.

Boerlin, M., Machens, C.K., and Denève, S. (2013). Predictive coding of dynamical variables in balanced spiking networks. PLoS Comput. Biol. *9*, e1003258.

Bolding, K.A., and Franks, K.M. (2017). Complementary codes for odor identity and intensity in olfactory cortex. eLife *6*, e22630.

Brunel, N. (2016). Is cortical connectivity optimized for storing information? Nat. Neurosci. *19*, 749–755.

Chapeton, J., Fares, T., LaSota, D., and Stepanyants, A. (2012). Efficient associative memory storage in cortical circuits of inhibitory and excitatory neurons. Proc. Natl. Acad. Sci. USA *109*, E3614–E3622.

Chapuis, J., and Wilson, D.A. (2011). Bidirectional plasticity of cortical pattern recognition and behavioral sensory acuity. Nat. Neurosci. *15*, 155–161.

Chiu, C.Q., Martenson, J.S., Yamazaki, M., Natsume, R., Sakimura, K., Tomita, S., Tavalin, S.J., and Higley, M.J. (2018). Input-specific NMDAR-dependent potentiation of dendritic GABAergic inhibition. Neuron *97*, 368–377.e363.

Choe, H.K., Reed, M.D., Benavidez, N., Montgomery, D., Soares, N., Yim, Y.S., and Choi, G.B. (2015). Oxytocin Mediates Entrainment of Sensory Stimuli to Social Cues of Opposing Valence. Neuron *87*, 152–163.

Choi, G.B., Stettler, D.D., Kallman, B.R., Bhaskar, S.T., Fleischmann, A., and Axel, R. (2011). Driving opposing behaviors with ensembles of piriform neurons. Cell *146*, 1004–1015.

D'amour, J.A., and Froemke, R.C. (2015). Inhibitory and excitatory spike-timing-dependent plasticity in the auditory cortex. Neuron *86*, 514–528.

Denève, S., and Machens, C.K. (2016). Efficient codes and balanced networks. Nat. Neurosci. *19*, 375–382.

Denève, S., Alemi, A., and Bourdoukan, R. (2017). The Brain as an Efficient and Robust Adaptive Learner. Neuron *94*, 969–977.

Dorrn, A.L., Yuan, K., Barker, A.J., Schreiner, C.E., and Froemke, R.C. (2010). Developmental sensory experience balances cortical excitation and inhibition. Nature *465*, 932–936.

Franks, K.M., Russo, M.J., Sosulski, D.L., Mulligan, A.A., Siegelbaum, S.A., and Axel, R. (2011). Recurrent circuitry dynamically shapes the activation of piriform cortex. Neuron *72*, 49–56.

Friedrich, R.W., and Korsching, S.I. (1997). Combinatorial and chemotopic odorant coding in the zebrafish olfactory bulb visualized by optical imaging. Neuron *18*, 737–752.

Friedrich, R.W., and Laurent, G. (2001). Dynamic optimization of odor representations by slow temporal patterning of mitral cell activity. Science *291*, 889–894.

Friedrich, R.W., Habermann, C.J., and Laurent, G. (2004). Multiplexing using synchrony in the zebrafish olfactory bulb. Nat. Neurosci. *7*, 862–871.

Froemke, R.C. (2015). Plasticity of cortical excitatory-inhibitory balance. Annu. Rev. Neurosci. *38*, 195–219.

Grosmaitre, X., Santarelli, L.C., Tan, J., Luo, M., and Ma, M. (2007). Dual functions of mammalian olfactory sensory neurons as odor detectors and mechanical sensors. Nat. Neurosci. *10*, 348–354.

Haberly, L.B. (2001). Parallel-distributed processing in olfactory cortex: new insights from morphological and physiological analysis of neuronal circuitry. Chem. Senses *26*, 551–576.

Hasselmo, M.E., and Barkai, E. (1995). Cholinergic modulation of activity-dependent synaptic plasticity in the piriform cortex and associative memory function in a network biophysical simulation. J. Neurosci. *15*, 6592–6604.

Hennequin, G., Vogels, T.P., and Gerstner, W. (2012). Non-normal amplification in random balanced neuronal networks. Phys. Rev. E Stat. Nonlin. Soft Matter Phys. *86*, 011909.

Hennequin, G., Vogels, T.P., and Gerstner, W. (2014). Optimal control of transient dynamics in balanced networks supports generation of complex movements. Neuron *82*, 1394–1406.

Hennequin, G., Agnes, E.J., and Vogels, T.P. (2017). Inhibitory Plasticity: Balance, Control, and Codependence. Annu. Rev. Neurosci. *40*, 557–579.

Hopfield, J.J. (1982). Neural networks and physical systems with emergent collective computational abilities. Proc. Natl. Acad. Sci. USA *79*, 2554–2558.

Hubel, D.H., and Wiesel, T.N. (1962). Receptive fields, binocular interaction and functional architecture in the cat's visual cortex. J. Physiol. *160*, 106–154.

Isaacson, J.S., and Scanziani, M. (2011). How inhibition shapes cortical activity. Neuron *72*, 231–243.

Iurilli, G., and Datta, S.R. (2017). Population coding in an innately relevant olfactory area. Neuron *93*, 1180–1197.e1187.https://www.ncbi.nlm.nih.gov/pubmed/28238549

Jacobson, G.A., Rupprecht, P., and Friedrich, R.W. (2018). Experience-dependent plasticity of odor representations in the telencephalon of zebrafish. Curr. Biol. *28*, 1–14.e13.

Kitamura, K., Judkewitz, B., Kano, M., Denk, W., and Häusser, M. (2008). Targeted patch-clamp recordings and single-cell electroporation of unlabeled neurons in vivo. Nat. Methods *5*, 61–67.

Large, A.M., Vogler, N.W., Mielo, S., and Oswald, A.M. (2016). Balanced feedforward inhibition and dominant recurrent inhibition in olfactory cortex. Proc. Natl. Acad. Sci. USA *113*, 2276–2281.

Li, J., Mack, J.A., Souren, M., Yaksi, E., Higashijima, S., Mione, M., Fetcho, J.R., and Friedrich, R.W. (2005). Early development of functional spatial maps in the zebrafish olfactory bulb. J. Neurosci. *25*, 5784–5795.

Litwin-Kumar, A., and Doiron, B. (2012). Slow dynamics and high variability in balanced cortical networks with clustered connections. Nat. Neurosci. *15*, 1498–1505.

Liu, B.H., Wu, G.K., Arbuckle, R., Tao, H.W., and Zhang, L.I. (2007). Defining cortical frequency tuning with recurrent excitatory circuitry. Nat. Neurosci. *10*, 1594–1600.

Longair, M.H., Baker, D.A., and Armstrong, J.D. (2011). Simple Neurite Tracer: open source software for reconstruction, visualization and analysis of neuronal processes. Bioinformatics *27*, 2453–2454.

Miura, K., Mainen, Z.F., and Uchida, N. (2012). Odor representations in olfactory cortex: distributed rate coding and decorrelated population activity. Neuron *74*, 1087–1098.

Miyamichi, K., Amat, F., Moussavi, F., Wang, C., Wickersham, I., Wall, N.R., Taniguchi, H., Tasic, B., Huang, Z.J., He, Z., et al. (2011). Cortical representations of olfactory input by trans-synaptic tracing. Nature *472*, 191–196.

Miyasaka, N., Arganda-Carreras, I., Wakisaka, N., Masuda, M., Sümbül, U., Seung, H.S., and Yoshihara, Y. (2014). Olfactory projectome in the zebrafish forebrain revealed by genetic single-neuron labelling. Nat. Commun. *5*, 3639.

Mueller, T., Dong, Z., Berberoglu, M.A., and Guo, S. (2011). The dorsal pallium in zebrafish, Danio rerio (Cyprinidae, Teleostei). Brain Res. *1381*, 95–105.

Murphy, B.K., and Miller, K.D. (2009). Balanced amplification: a new mechanism of selective amplification of neural activity patterns. Neuron *61*, 635–648.

Okun, M., and Lampl, I. (2008). Instantaneous correlation of excitation and inhibition during ongoing and sensory-evoked activities. Nat. Neurosci. *11*, 535–537.

Oswald, A.M., Schiff, M.L., and Reyes, A.D. (2006). Synaptic mechanisms underlying auditory processing. Curr. Opin. Neurobiol. *16*, 371–376.

Pologruto, T.A., Sabatini, B.L., and Svoboda, K. (2003). ScanImage: flexible software for operating laser scanning microscopes. Biomed. Eng. Online *2*, 13.

Poo, C., and Isaacson, J.S. (2009). Odor representations in olfactory cortex: "sparse" coding, global inhibition, and oscillations. Neuron *62*, 850–861.

Poo, C., and Isaacson, J.S. (2011). A major role for intracortical circuits in the strength and tuning of odor-evoked excitation in olfactory cortex. Neuron *72*, 41–48.

Renart, A., de la Rocha, J., Bartho, P., Hollender, L., Parga, N., Reyes, A., and Harris, K.D. (2010). The asynchronous state in cortical circuits. Science *327*, 587–590.

Roland, B., Deneux, T., Franks, K.M., Bathellier, B., and Fleischmann, A. (2017). Odor identity coding by distributed ensembles of neurons in the mouse olfactory cortex. eLife *6*, e26337.

Rubin, R., Abbott, L.F., and Sompolinsky, H. (2017). Balanced excitation and inhibition are required for high-capacity, noise-robust neuronal selectivity. Proc. Natl. Acad. Sci. USA *114*, E9366–E9375.

Rupprecht, P., Prendergast, A., Wyart, C., and Friedrich, R.W. (2016). Remote z-scanning with a macroscopic voice coil motor for fast 3D multiphoton laser scanning microscopy. Biomed. Opt. Express *7*, 1656–1671.

Schmidt, H., Gour, A., Straehle, J., Boergens, K.M., Brecht, M., and Helmstaedter, M. (2017). Axonal synapse sorting in medial entorhinal cortex. Nature *549*, 469–475.

Shadlen, M.N., and Newsome, W.T. (1994). Noise, neural codes and cortical organization. Curr. Opin. Neurobiol. *4*, 569–579.

Shu, Y., Hasenstaub, A., and McCormick, D.A. (2003). Turning on and off recurrent balanced cortical activity. Nature *423*, 288–293.

Sosulski, D.L., Bloom, M.L., Cutforth, T., Axel, R., and Datta, S.R. (2011). Distinct representations of olfactory information in different cortical centres. Nature *472*, 213–216.

Stettler, D.D., and Axel, R. (2009). Representations of odor in the piriform cortex. Neuron *63*, 854–864.

Stokes, C.C., and Isaacson, J.S. (2010). From dendrite to soma: dynamic routing of inhibition by complementary interneuron microcircuits in olfactory cortex. Neuron *67*, 452–465.

Sun, Y.J., Wu, G.K., Liu, B.H., Li, P., Zhou, M., Xiao, Z., Tao, H.W., and Zhang, L.I. (2010). Fine-tuning of pre-balanced excitation and inhibition during auditory cortical development. Nature *465*, 927–931.

Suter, B.A., O'Connor, T., Iyer, V., Petreanu, L.T., Hooks, B.M., Kiritani, T., Svoboda, K., and Shepherd, G.M.G. (2010). Ephus: multipurpose data acquisition software for neuroscience experiments. Front. Neural Circuits *4*, 100.

Tabor, R., Yaksi, E., Weislogel, J.M., and Friedrich, R.W. (2004). Processing of odor mixtures in the zebrafish olfactory bulb. J. Neurosci. *24*, 6611–6620.

Tan, A.Y., Zhang, L.I., Merzenich, M.M., and Schreiner, C.E. (2004). Tone-evoked excitatory and inhibitory synaptic conductances of primary auditory cortex neurons. J. Neurophysiol. *92*, 630–643.

Tan, A.Y., Brown, B.D., Scholl, B., Mohanty, D., and Priebe, N.J. (2011). Orientation selectivity of synaptic input to neurons in mouse and cat primary visual cortex. J. Neurosci. *31*, 12339–12350.

van Vreeswijk, C., and Sompolinsky, H. (1996). Chaos in neuronal networks with balanced excitatory and inhibitory activity. Science *274*, 1724–1726.

Vogels, T.P., Sprekeler, H., Zenke, F., Clopath, C., and Gerstner, W. (2011). Inhibitory plasticity balances excitation and inhibition in sensory pathways and memory networks. Science *334*, 1569–1573.

Wehr, M., and Zador, A.M. (2003). Balanced inhibition underlies tuning and sharpens spike timing in auditory cortex. Nature *426*, 442–446.

Wilent, W.B., and Contreras, D. (2005). Dynamics of excitation and inhibition underlying stimulus selectivity in rat somatosensory cortex. Nat. Neurosci. *8*, 1364–1370.

Wilson, D.A., and Sullivan, R.M. (2011). Cortical processing of odor objects. Neuron *72*, 506–519.

Wullimann, M.F., Rupp, B., and Reichert, H. (1996). Neuroanatomy of the zebrafish brain: a topological atlas (Basel: Birkhäuser).

Xue, M., Atallah, B.V., and Scanziani, M. (2014). Equalizing excitation-inhibition ratios across visual cortical neurons. Nature *511*, 596–600.

Yaksi, E., von Saint Paul, F., Niessing, J., Bundschuh, S.T., and Friedrich, R.W. (2009). Transformation of odor representations in target areas of the olfactory bulb. Nat. Neurosci. *12*, 474–482.

Yamauchi, T., Hori, T., and Takahashi, T. (2000). Presynaptic inhibition by muscimol through GABAB receptors. Eur. J. Neurosci. *12*, 3433–3436.

Zhu, P., Fajardo, O., Shum, J., Zhang Schärer, Y.-P., and Friedrich, R.W. (2012). High-resolution optical control of spatiotemporal neuronal activity patterns in zebrafish using a digital micromirror device. Nat. Protoc. *7*, 1410–1425.

Please cite this article in press as: Rupprecht and Friedrich, Precise Synaptic Balance in the Zebrafish Homolog of Olfactory Cortex, Neuron (2018), https://doi.org/10.1016/j.neuron.2018.09.013

STAR★METHODS

KEY RESOURCES TABLE

REAGENT or RESOURCE	SOURCE	IDENTIFIER
Chemicals, Peptides, and Recombinant Proteins		
Muscimol, BODIPY TMR-X Conjugate	Thermo Fisher	Cat#M23400
QX-314	Sigma-Aldrich	Cat#L5783
SCH50911	Tocris Bioscience	Cat#0984
Experimental Models: Organisms/Strains		
Zebrafish transgenic line, neuroD:GCaMP6f	Rupprecht et al., 2016	N/A
Zebrafish transgenic line, elavl3:GCaMP5	Ahrens et al., 2013	N/A
Zebrafish wildtype line, AbEK/TÜ x WIK	Jacobson et al., 2018	N/A
Software and Algorithms		
MATLAB 2013a; MATLAB 2014a	The Mathworks	RRID:SCR_001622; http://www.mathworks.com/products/matlab/
R 3.4.3	R Foundation for Statistical Computing	RRID:SCR_001905; http://www.r-project.org/
Python 3.6	Python Programming Language	RRID:SCR_008394; http://www.python.org/
Software for ROI analysis of calcium imaging data	This paper	RRID:SCR_016352; https://git.io/vAeKZ
Deep convolutional networks for spike probability prediction with Python and Keras	Berens et al., 2018	RRID:SCR_016354; https://git.io/vNbsz
MATLAB control software for Reglo ICC peristaltic pumps	This paper	RRID:SCR_016353; https://git.io/vymwn
Other		
Two-photon resonant microscope for multi-plane imaging	Rupprecht et al., 2016	DOI:10.1364/BOE.7.001656

CONTACT FOR REAGENT AND RESOURCE SHARING

Further information and requests for resources and reagents should be directed to and will be fulfilled by the Lead Contact, Rainer Friedrich (Rainer.Friedrich@fmi.ch).

EXPERIMENTAL MODEL AND SUBJECT DETAILS

Experiments were performed in healthy adult (5 - 12 month old) zebrafish (*Danio rerio*) of both sexes. Fish from both sexes were combined because sex-specific differences were not examined in this study. Fish were raised and kept under standard laboratory conditions (26 – 27°C; 13 h/11 h light/dark cycle). Electrophysiological recordings and calcium imaging in Dp were performed in a neuroD:GCaMP6f transgenic line that expresses the genetically encoded calcium indicator GCaMP6f in most neurons of the dorsal pallium and in all neurons of Dp (Rupprecht et al., 2016). Dye fillings were performed either in the same transgenic line or in a wild-type line (AbEK/TÜ x WIK). Calcium imaging in the OB was performed as described (Jacobson et al., 2018) in an elavl3:GCaMP5 transgenic line (Ahrens et al., 2013) that expresses GCaMP5 predominantly or exclusively in mitral cells of the adult OB (Li et al., 2005). All experiments were approved by the Veterinary Department of the Canton Basel-Stadt (Switzerland).

METHOD DETAILS

Surgery for *ex vivo* experiments

Physiological measurements were performed in an *ex vivo* preparation of the entire zebrafish brain and nose (Zhu et al., 2012). Briefly, fish were anesthetized by cooling to 4°C and decapitated in artificial cerebrospinal fluid (ACSF) containing (in mM) 124 NaCl, 2 KCl, 1.25 KH_2PO_4, 1.6 $MgSO_4$, 22 D-(+)-Glucose, 2 $CaCl_2$, 24 $NaHCO_3$, pH 7.2. After dissection of the jaws, the eyes and the bones covering the ventral telencephalon, the dura mater over the posterior zone of the dorsal telencephalon (Dp) was removed with

fine forceps. For experiments in the OB, the ventral bones covering the OB were also removed. After surgery, the preparation was placed in a perfusion chamber and slowly warmed up to room temperature.

Odor application

Amino acids (final concentration: 40 μM; Sigma Aldrich) and a bile acid (taurodeoxycholic acid [TDCA]; final concentration: 4 μM; Sigma Aldrich) were prepared as 100x stock solutions in double-distilled water, vortexed, sonicated, stored at −20°C and diluted to the final concentration in ACSF immediately before the experiment. Food odor was prepared as described (Tabor et al., 2004). Odors were applied through a constant stream of ACSF directed at the ipsilateral naris. The total flow rate was held constant at 5 mL/min by a 4-wheel peristaltic pump (Reglo ICC, Ismatec). The wheels controlled independent lines for ACSF and three different odor solutions that were merged downstream by three-way junctions. The speeds of the four pump wheels were controlled independently via a serial port using a custom-written MATLAB interface (https://git.io/vymwn). This setup permitted precisely timed applications of three different odors at arbitrary concentrations, stimulus durations and combinations. Inter-stimulus intervals (ISIs) were > 1 min.

Electrophysiology

Voltage clamp recordings were performed using borosilicate pipettes (4 – 8 MΩ pipette resistance for pDp, 5 – 10 MΩ for aDp, 10 – 15 MΩ for NT), a Multiclamp 700B amplifier (Molecular Devices) and Ephus software (Suter et al., 2010). Pipettes were filled with an intracellular solution containing (in mM) 132 Cs methane sulfonate, 10 Na_2-phosphocreatine, 4 $MgCl_2$, 4 Na_2-ATP, 0.4 Na-GTP, 5 L-glutathione, 0.1 EGTA, 10 HEPES (pH 7.2, 300 mOsm; all Sigma). Current clamp recordings and voltage clamp recordings without Cs were performed with an intracellular solution that contained (in mM): 129 K-gluconate, 10 HEPES (free acid), 0.1 EGTA, 4 Na_2-ATP, 10 Na_2-phosphocreatine, 0.3 Na-GTP, 5 L-glutathione and 13.1 KOH (pH 7.2, 305 mOsm; all Sigma). For voltage clamp experiments at multiple holding potentials between −70 mV and 0 mV, 2 mM QX-314 (Sigma) was included in the internal solution to block voltage-dependent cation channels in the recorded cell only.

Neurons were targeted by the shadow-patching technique (Kitamura et al., 2008) with 0.05 mM Alexa488 or Alexa594 (Invitrogen) in the internal solution using a custom-designed video-rate multiphoton microscope (Rupprecht et al., 2016; see also Methods Video S1). When the dura mater over Dp was not completely removed the pipette was advanced through the dura mater with transient high pressure (100 mbar) to avoid contamination of the pipette tip. Before making a seal, neurons were approached inside the tissue with low pressure (20 mbar). After break-in, series resistance and input resistance were continuously monitored. On average, neurons were recorded for 27 ± 11 min. LFP recordings were performed in the deep layers of the OB (Friedrich et al., 2004) ipsilateral to the whole-cell recording in Dp using pipettes filled with ACSF (6 – 8 MΩ).

Mapping of neuron positions onto a reference stack

A stack of transverse multiphoton images covering Dp was obtained from the intact brain of a neuroD:GCaMP6f transgenic fish (Rupprecht et al., 2016) within a bounding box of 680 × 420 × 390 μm^3 (rostro-caudal x medio-lateral x ventro-dorsal; resolution: 0.41 μm lateral pixel size, 2.5 μm axial step size). A stack of sagittal images was subsequently acquired from the same brain volume after turning the sample by 90 degrees. Both views were then mapped into a common coordinate system to obtain high-resolution views of the telencephalic surface from multiple directions (Figures 1A and 1B; Video S1).

Most experiments were performed using the same neuroD:GCaMP6f line as for the reference stack. Prior to patch clamp recordings, multiphoton calcium imaging was performed to verify that odor stimulation evoked responses in Dp. After each whole-cell recording, an image stack was acquired that covered the local environment of the recorded neuron (20 – 30 sections spaced by 2.5 μm). After the last recording, a stack covering the full volume of Dp was acquired (150 – 200 sections spaced by 2.5 μm). Mapping of individual neurons onto the reference stack was then performed manually.

Temporal alignment of voltage clamp recordings

The delay between the trigger signal for odor delivery and the arrival of the odor solution at the naris was approximately 2 s. In order to verify the reproducibility of odor delivery we used volumetric two-photon imaging (4 planes, volume rate of 7.5 Hz) to detect the arrival of a fluorescein solution. These measurements revealed no detectable variation in stimulus onset between trials in the same experiment. However, small variations may occur between experiments performed on different days due to variable positioning of the ACSF/odor tube outlet relative to the naris and other factors such as wear of tubing. We therefore aligned results from different experiments on the earliest observation of an odor response in each experiment. No further alignment was performed among trials in the same experiment. To determine the response onset time in a given experiment, responses of all responses to all odors were considered. The onset was determined as the time point when the fastest-responding neuron-odor pair reached 15% of its maximum value. This procedure was manually supervised.

The average delay between the stimulus trigger and the response onset was 1.94 ± 0.38 s (mean ± SD across experiments). Hence, the variability in response onset times was small relative to the temporal resolution of most of our analysis. Note that analyses with very high temporal resolution did not depend on the precise stimulus onset because the LFP oscillation in the OB was used as a clock signal.

Some neurons in pDp responded not only to odor stimuli but also to changes in flow, consistent with the mechanosensitivity of olfactory sensory neurons (Grosmaitre et al., 2007). Small transient flow changes occurred when flow rates were changed in the different odor lines, even though the total flow rate was kept constant in the steady-state. However, these flow changes occurred ~2 s before the arrival of the odor at the nose (see Figure 2D). Small responses to flow changes could therefore be separated in time from responses to the odor. The baseline activity that was subtracted for further analysis (Figure 2D, Figure 5B) was measured in the time window that preceded these flow-evoked input currents (up to 2.5 s before odor response onset).

Analysis of biophysical properties of neurons

Biophysical properties were analyzed using voltage steps (50 ms; $\Delta V = -5$ mV; ISI = 100 ms) that were applied at a holding potential of −70 mV. The asymptotic current $I_{asymptote}$ after the capacitive transient was used to calculate the input resistance $R_{in} = \Delta V/(I_{median} - I_{asymptote})$. I_{median} was the median current during 50 ms preceding the test pulse. The same procedure was applied before break-in to measure the seal resistance R_{seal}. Measurements were averaged over 20 test pulses with an ISI of 100 ms. In most neurons, this protocol was performed after each odor stimulation. The same recordings were used to estimate the membrane time constants $\tau_m = C_m \times R_m$. R_{in} was used as a proxy for R_m, and C_m was determined by integrating the charge accumulated during the falling phase of the capacitive transient. For measurements of input resistance during the odor response (Figure 4E), I_{median} was computed by averaging median currents during the two 50 ms windows surrounding the test pulse.

Estimates of the membrane resistance neglect the seal resistance R_{seal} and therefore underestimate R_{in}. To estimate the resulting error we measured R_{seal} in 15 neurons of pDp before break-in and subsequently measured R_{in} after break-in. On average, the error made by neglecting R_{seal} was 25 ± 5% of the measured value (Figure S5A). This is probably a conservative estimate because R_{seal} may decrease after break-in. The odor-evoked conductance change was underestimated accordingly.

Tracing of neurites

To visualize neuronal morphology on the background fluorescence of the transgenic neuroD:GCaMP6f line the concentration of the dye in the intracellular solution (sulforhodamine 101 or Alexa488) was increased to 0.2 – 0.5 mM. The osmolality of the intracellular solution was increased by ca. 2%, which lead to a swelling of the neuron especially at bifurcation points of the dendrites and facilitated subsequent tracing. After > 10 min post break-in an image stack was acquired at high resolution (0.2 – 0.4 μm lateral pixel size, 1 μm axial step size), typically with > 350 sections and extensive averaging. If the respective neuron appeared to be very small, acquisition of the stack was repeated > 30 min later. In none of these cases, additional neurite trees were recovered. At most one pDp, NT and aDp neuron each was filled in a single fish in order to prevent ambiguity of tracings through overlapping neurites. Tracings were performed using the Simple Neurite Tracer (Longair et al., 2011) and subsequently processed in MATLAB to align the skeletons to the reference stack.

The volume V of the convex hull was calculated to compute the equivalent spherical diameter of the dendritic tree, $d_{equivalent} = 2 \cdot \sqrt[3]{3/(4\pi) \cdot V}$. In a basic Sholl analysis, neurite length was quantified in 10 μm radial shells around the soma for each neuron and averaged across neurons.

Muscimol and SCH50911 injection

Muscimol (Thermo Fisher) was dissolved in ACSF (5 mM) and pressure-injected into Dp of neuroD:GCaMP6f transgenic fish. For experiments using a cocktail of muscimol and SCH50911 (Tocris), muscimol (5 mM) and SCH50911 (7.5 mM) were dissolved in ACSF and co-injected into Dp. The ratio (1:1.5) followed established protocols to ensure blockade of $GABA_B$ but not $GABA_A$ receptors (Liu et al., 2007). 0.05 mM Alexa 594 was included in the injection pipette to target the injection and to visualize the spread by multiphoton microscopy. Typically, three injections were placed in aDp, in pDp and at the interface between pDp and NT. Electrophysiological experiments were performed within 60 min after injection and absence of spiking activity in Dp was verified by calcium imaging. Despite the absence of calcium signals, all recorded neurons exhibited spontaneous or evoked EPSC events and a fast voltage-dependent conductance that was engaged by depolarization to ca. −40 mV.

Calcium imaging experiments

Multiphoton calcium imaging in the OB was performed using a resonant scanning multiphoton microscope equipped with a remote focusing unit that takes advantage of a voice coil motor for fast z-scanning (Rupprecht et al., 2016). To increase the mitral cell imaging yield within a trial, 4 or 8 focal planes with 512 × 512 or 512 × 256 pixels each were imaged simultaneously at a frame rate of 7.5 Hz. Calcium imaging in Dp was performed using the same microscope but in a single optical section (1024 × 1024 pixels; frame rate, 15.4 Hz). The microscope was controlled by a scanimage software (Pologruto et al., 2003) with some modifications (Rupprecht et al., 2016).

QUANTIFICATION AND STATISTICAL ANALYSIS

Co-tuning analysis for pDp neurons

To correct for the fact that different stimuli have different strengths we first assumed that the magnitudes of synaptic currents evoked by an odor in a given neuron depend not only on the tuning of the neuron toward this stimulus (odor identity) but also on the global "stimulus strength" s of this stimulus relative to other stimuli, and on the total input received by the neuron ("neuronal size" n). The

response current r_{ij} in neuron i evoked by stimulus j was thus expressed as a product of the stimulus strength s_j, the neuron-specific input strength n_i, and additional variability v_{ij} that accounts for other factors including tuning and noise:

$$r_{ij} = s_j \cdot n_i \cdot v_{ij}$$

This linear expression is a heuristic procedure to jointly determine the best parameter estimates s_i and n_j with as few assumptions as possible. The projections of r_{ij} onto the balanced and counter-balanced axes for each neuron are plotted in Figure 6D.

Because $r_{ij,exp}$ was determined experimentally we estimated the input strength n_i of each neuron and the intrinsic strength s_j of each stimulus jointly by minimizing

$$\sum_{ij} (r_{ij,exp} - s_j \cdot n_i)^2$$

The normalized responses for neuron i and stimulus j

$$EPSC_{ij,norm} = EPSC_{ij,exp} / s_j$$

$$IPSC_{ij,norm} = IPSC_{ij,exp} / s_j$$

were computed to operate in a normalized space that is corrected for stimulus strength. In this space, projection of $EPSC_{ij,norm}$ and $IPSC_{ij,norm}$ of individual neurons onto the balanced and counter-balanced axes (Figure 6F) allowed for the quantification of co-tuning independent of stimulus strength and neuronal size.

Cross-correlation of simultaneous recordings

To measure the phase relationship between the oscillatory components of EPSCs, IPSCs and the LFP we band-pass filtered all recordings using a non-causal, phase-preserving filter (15 – 40 Hz). Auto- and cross-correlograms were calculated using a moving window of 100 ms and averaged over a 250 ms time window that spanned the oscillatory response phase (Figure 7G). Averaging across trials returned cross-correlation functions for EPSC-LFP and IPSC-LFP. The delay between EPSCs and IPSCs was then determined as the relative time shift of these cross-correlation functions. To determine the uncertainty of this measurement we quantified the same delay between two equally large, non-overlapping subsets of IPSC or EPSC trials of the same neuron and determined the standard error of the mean of the resulting distribution.

Detection of events for aDp recordings

To detect events in voltage clamp recordings from aDp neurons traces sampled at 10 kHz were median-filtered within a sliding 2 ms-window. Candidate events were then identified as at least three consecutive samples with a positive first derivative followed by at least two consecutive samples with negative derivative. Candidates were accepted or discarded based on two conditions: (1) the mean current in a 7 ms-window around the candidate time point of the high-pass filtered EPSC trace (cut-off frequency 0.25 Hz) must exceed the standard deviation of the full trace times a fudge factor F_1. (2) The mean of the first derivative of the EPSC trace, weighted with opposite signs before and after the candidate time point, must together exceed the standard deviation of the derivative of the trace times a fudge factor F_2. The fudge factors were chosen empirically and constant for all traces ($F_1 = 0.4$, $F_2 = 1.25$). This resulted in reliable detection of events, with few false negatives and very few false positives (Figure S7F). All detected events were subsequently visually inspected.

Power analysis in the 20-30 Hz band

For recordings from pDp neurons in muscimol and under control conditions (Figure 3G), the average power in the frequency range of 20 – 30 Hz was measured within the 500 ms response window during the first 1.5 s of the odor response that maximized the power for each neuron. Since the oscillatory power varies considerably between fish (not shown), we normalized the datasets with respect to the mean of the respective control condition (Figure 3G).

Analysis of calcium imaging experiments

Regions of interest (ROIs) corresponding to mitral cells or Dp neurons were drawn manually using a custom interactive MATLAB script (https://git.io/vAeKZ). Fluorescence was averaged over all pixels in a ROI. F_0 was calculated by taking the minimum value of each recording after smoothing with a 4 s running average. To infer spiking activity, $\Delta F/F_0$ traces were deconvolved using state-of-the-art methods based on convolutional neuronal networks for Dp recordings (https://git.io/vNbsz; (Berens et al., 2018)).

Decorrelation and stability analysis in the OB

To analyze odor representations across mitral cells in the OB we calculated the Pearson correlation coefficient between the activity patterns evoked by the same or by different stimuli at each time point. Measurements were averaged by weighing them according to the number of neurons that contributed to each pattern.

Statistical analysis

All statistical tests comparing two distributions were performed using the Wilcoxon rank-sum test; the corresponding effect sizes and confidence intervals were computed in *R* using the Hodges–Lehmann estimator. In all boxplots the central line indicates the median, edges indicate the 25th and 75th percentiles, and whiskers indicate most extreme data points except for outliers, which are defined as data points outside of 99.3% data coverage (assuming normally distributed data).

DATA AND SOFTWARE AVAILABILITY

The data that support the findings of this study are available from the Lead Contact upon request (rainer.friedrich@fmi.ch).

Software that has been generated for this study is available on Github (see Key Resources Table).